Bull Volcanol
DOI 10.1007/s00445-012-0580-6

RESEARCH ARTICLE

Magma storage conditions beneath Dabbahu Volcano (Ethiopia) constrained by petrology, seismicity and satellite geodesy

L. Field · J. Blundy · R. A. Brooker · T. Wright · G. Yirgu

Received: 26 March 2011 / Accepted: 28 January 2012

Abstract A variety of methods exist to constrain subvolcanic storage conditions of magmas. Petrological, seismological and satellite geodetic methods are integrated to determine storage conditions of peralkaline magmas beneath Dabbahu Volcano, Afar, Ethiopia. Secondary ion mass spectrometry (SIMS) analysis of volatile contents in melt inclusions trapped within phenocrysts of alkali feldspar, clinopyroxene and olivine from pantellerite obsidians representing the youngest eruptive phase (<8 ka) show H_2O contents ≤5.8 wt.% and CO_2 contents generally below 500 ppm, although rarely as high as 1,500 ppm. Volatile saturation pressures (at 679–835°C) are in the range 43–207 MPa, consistent with published experimental data for similar pantellerites, which show that the phenocryst assemblage of alkali feldspar + cpx + aenigmatite ± ilmenite is stable at 100 to 150 MPa. Inferred magma storage depths for these historic eruptions are ~1–5 km below sea-level, consistent with the depths of earthquakes, associated with magma chamber deflation following a dyke intrusion in the period Oct 2005–Apr 2006. Interferometric synthetic aperture radar (InSAR) data for the same period reveal a broad ~20 km diameter area of uplift. Modelling of different geometries reveals that a series of stacked sills over a 1–5 km depth range best matches the InSAR data. The consistency of depth estimates based on petrological study of ancient eruptions and the seismicity, inflation and deflation of Dabbahu observed in relation to the dyking event of 2005, suggest a small but vertically extensive and potentially long-lived magma storage region.

Keywords Melt inclusions · Afar · Magma storage · Dabbahu · Volatiles · InSAR · Peralkaline

Editorial responsibility: M. Ripepe

Electronic supplementary material The online version of this article (doi:10.1007/s00445-012-0580-6) contains supplementary material, which is available to authorized users.

L. Field (✉) · J. Blundy · R. A. Brooker
School of Earth Sciences, University of Bristol,
Wills Memorial Building, Queen's Road,
Bristol BS8 1RJ, UK
e-mail: Lorraine.Field@bristol.ac.uk

J. Blundy
e-mail: jon.blundy@bristol.ac.uk

T. Wright
School of Earth and Environment, University of Leeds,
Leeds LS2 9JT, UK

G. Yirgu
Department of Earth Sciences, University of Addis Ababa,
Addis Ababa, Ethiopia

Introduction

Dabbahu volcano is situated in a remote area of northern Ethiopia with almost no documented eruptions. In this study, we attempt to further our understanding of the magma storage beneath Dabbahu volcano and thus future eruptions, by integrating three lines of evidence: petrology, seismicity and interferometric synthetic aperture radar (InSAR). Although active fumaroles, seismicity and InSAR evidence of inflation and deflation centred beneath Dabbahu indicate the volcano is active, there are no recorded eruptions of Dabbahu itself in historical times. However, evidence shows that large eruptions have occurred during its history. Constraining magma storage depths is critical in evaluating likely eruption styles and mitigating volcanic hazard and yet is notoriously hard to do remotely. Petrological methods for constraining magma storage depths (Blundy and Cashman 2008) include measurement of dissolved volatiles

Published online: 26 February 2012

(principally H_2O and CO_2) in phenocryst-hosted melt inclusions (MI), from which saturation pressures are calculated using solubility models. These methods are a posteriori in that they require erupted materials and thus can determine where magma was stored prior to the last eruption, but this need not be the same as current magma storage depths. Petrological methods rely on a magma being volatile-saturated which needs to be independently evaluated, on reliable pressure–solubility models as solubility is composition-sensitive and temperature-dependent, and on suitable crustal density models for pressure–depth conversion. Finally, further complications may occur from post-entrapment volatile leakage from MI or diffusive loss of volatiles through the host mineral.

An alternative means of prospecting for un-erupted magma is to deploy dense arrays of seismometers to record local or teleseismic events and use precisely located local earthquakes to define the outer margins of a magma body or construct full tomographic inversions (e.g. Lees 2007; Shalev et al. 2010). Magnetotelluric methods are sensitive to the presence of shallow highly conductive magma layers (e.g. Hill et al. 2009; Whaler and Hautot 2006), but data acquisition is time-consuming and expensive and the presence of a shallow, non-magmatic layer such as an aquifer can reduce depth resolution. Gravity measurements provide robust means of imaging sub-crustal density, but in isolation can only identify low-density bodies, rather than magma per se. Repeated gravity surveys have been used successfully to track the migration of density anomalies and hence infer sub-volcanic magma movement (e.g. Williams-Jones et al. 2008).

InSAR is a tool that enables surface deformation to be mapped with high precision and high spatial resolution remotely (Bürgmann et al. 2000; Wright 2002). InSAR has recently been used in the Andes to identify areas of active upwelling, thought to correspond to recharge of the crustal magma storage regions (Pritchard and Simons 2002). Reconstructing magma storage depths from InSAR is not straightforward because of the uncertainties that accompany the rheological behaviour of crustal rocks surrounding the magma body and simple models, e.g. such as those of Mogi (e.g. Sasai 1991), cannot capture the complexities of the natural situation. The geometry of the magma body and the rheology of the wall-rocks also influence the observed deformation pattern. Careful matching of observed and modelled deformation patterns, such as that performed by (Wright et al. 2006), serves to increase confidence in estimated magma storage depths, but such solutions are inherently non-unique.

In this paper, we combine petrological, seismic and InSAR methods of estimating magma storage conditions beneath an active volcano in the remote Afar region of northern Ethiopia. The petrological estimates are derived from the youngest, peralkaline rhyolites erupted from Dabbahu volcano (<8 ka), whereas seismicity and InSAR data pertain to on-going tectono-magmatic activity in the area. Our principal objective is to establish whether current patterns of unrest are consistent with previous, pre-eruptive magma storage conditions. To our knowledge, this is the first time that these three approaches have been combined to constrain magma storage depths beneath an active volcano.

Geological background

Dabbahu is a Quaternary volcano situated at the northern end of the Manda Hararo rift segment (MHRS) in the Afar region of Ethiopia (12° 39′39.24″ N, 40° 28′45.10″ E) (Fig. 1). The Afar depression at the triple junction between the Red Sea, Gulf of Aden and East African rift has been produced by rifting of Arabia away from the African continent over the past ~30 million years (Myr) (Wolfenden et al. 2005). The southern Red Sea rift has become segmented over the past ~3 Myr with the development of ~60 km long magmatic segments as faulting and volcanic activity has become more focused into localised regions (Barberi and Varet 1977).

The MHRS, a 35 km wide central depression interspersed with silicic edifices (Lahitte et al. 2003), comprises the currently active Dabbahu magmatic segment (DMS) to the north and the adjacent Hararo segment to the south (Rowland et al. 2007). The DMS includes a dissected silicic complex known as the Ado'Ale Volcanic Complex (AVC) ~30 km SSE of Dabbahu. Known also as Boina, Dabbahu is a ~1,400 m high central volcano rising from a base of fissural basalts and considered an example of a full fractional crystallisation suite from mildly alkaline basalts to peralkaline rhyolites (Barberi et al. 1974a, b; Bizouard et al. 1980). The youngest volcanic rocks at Dabbahu are peralkaline rhyolitic obsidians (Barberi et al. 1974a), characterised by molar $(Na_2O+ K_2O)/Al_2O_3$ >1, (NK/A), which can be further sub-divided into comendites and pantellerites (Macdonald 1974). These lavas have formed the distinctive NW and summit flows (Fig. 1a) up to ~8 m high with pantellerite flows overlying the comendite flows. Both comendites and pantellerites are found as lava flows and in the form of explosive tephras. Individual flow sizes vary from tiny (<0.001 m^3) to ~0.13 km^3. A small rhyolitic ash eruption occurred ~7 km from Dabbahu summit at the Da'Ure vent (12° 39′00.58″ N, 40° 31′10.43″ E) in 2005, the first documented historical eruption in this area, which coincided with the largest dyke opening event ever

Fig. 1 **a** Sample locality (satellite image courtesy of Sophie Hautot). The prominent *dark flows* in the NW and around the summit are obsidians and represent the youngest volcanic activity in the area. *Numbers* in *red* denote samples used for melt inclusion analysis, those in *white*, matrix glass analysis. **b** Location map of Dabbahu and the Manda Hararo Rift Segment (*MHRS*). **c** Simplified geological map based on Barberi et al. (1974a)

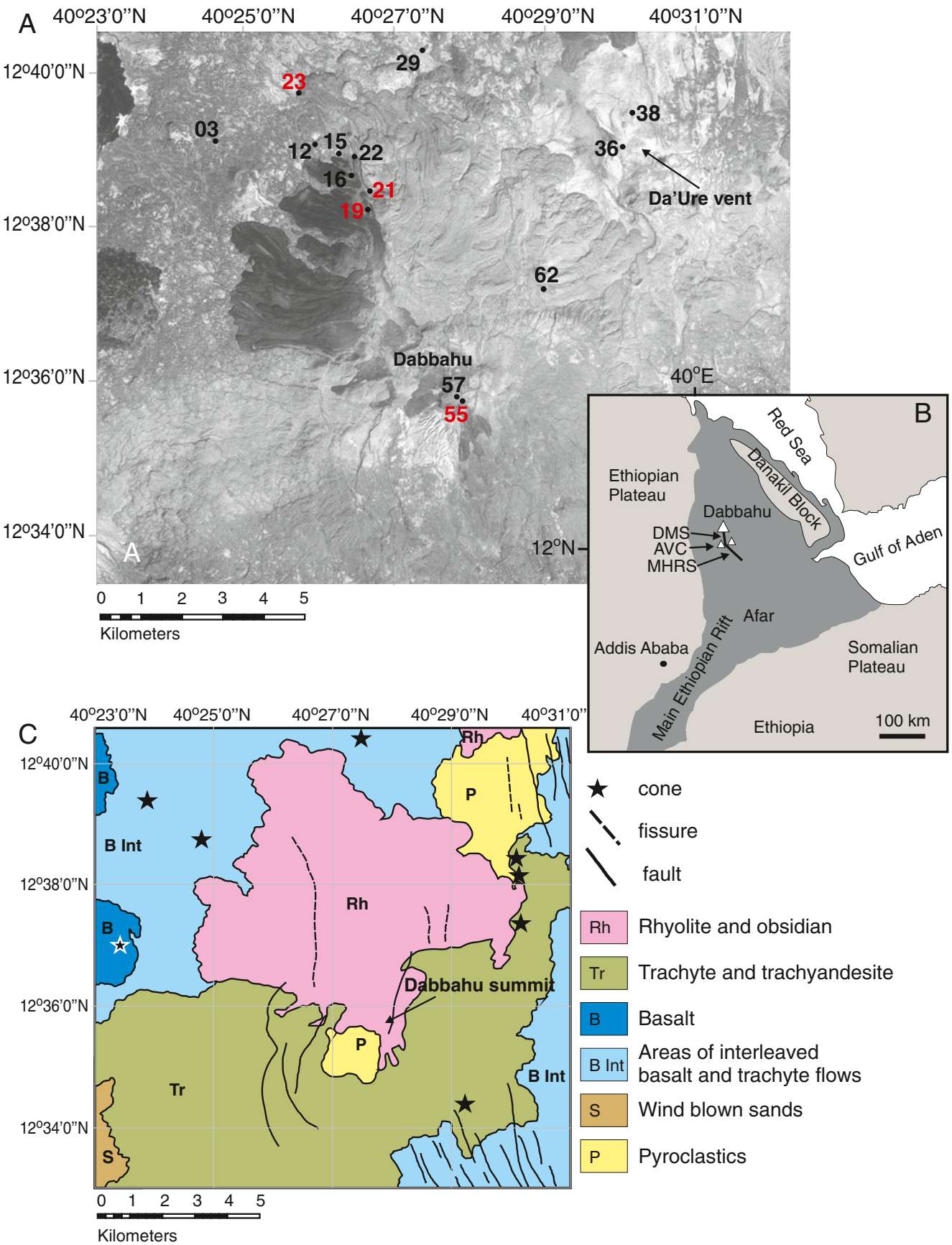
A
40°23'0"N
40°25'0"N
40°27'0"N
40°29'0"N
40°31'0"N
12°40'0"N
12°38'0"N
12°36'0"N
12°34'0"N
29
23
03
38
36
12
15
22
16
21
19
62
Da'Ure vent
Dabbahu
57
55
A
0 1 2 3 4 5
Kilometers
40°E
12°N
B
Red Sea
Danakil Block
Ethiopian Plateau
Dabbahu
DMS
AVC
MHRS
Gulf of Aden
Afar
Addis Ababa
Somalian Plateau
Main Ethiopian Rift
Ethiopia
100 km
C
40°23'0"N
40°25'0"N
40°27'0"N
40°29'0"N
40°31'0"
12°40'0"N
12°38'0"N
12°36'0"N
12°34'0"N
B
B Int
Rh
P
Tr
S
Dabbahu summit
0 1 2 3 4 5
Kilometers
cone
fissure
fault
Rhyolite and obsidian
Trachyte and trachyandesite
Basalt
Areas of interleaved basalt and trachyte flows
Wind blown sands
Pyroclastics

measured (~60 km) and the first such event in the modern age of satellite geodetic methods (Ayele et al. 2007). Modelled as a basaltic dyke at ~10 km depth (Wright et al. 2006), analysis suggests the dyke was sourced from three locations: the Dabbahu and Gab'ho volcanic complexes and the third major source at the AVC south of Dabbahu (Ayele et al. 2009).

Samples studied

We analysed matrix glasses from pumices and rhyolite obsidian flows and glassy MI from four rhyolite obsidians, collected from Dabbahu during field campaigns in 2008 and 2009. Samples 019, 021, 023 and 055 are from some of the youngest flows on Dabbahu; sample 055 is from the summit area. These obsidian rhyolites are phenocryst-poor, e.g. the most crystal-rich sample used (sample 055) contains just 7 vol.% phenocrysts. Crystals are generally discrete, although a few glomerocrysts are present. The dominant phenocryst assemblage from these samples is alkali feldspar + clinopyroxene + apatite, with alkali feldspar being the most abundant phenocryst. Feldspar and clinopyroxene form euhedral to subhedral crystals; feldspars are large (up to 1.5 mm) compared with clinopyroxenes (up to 200 μm). Fayalite, aenigmatite and ilmenite crystals are also found in the samples, together with rare amphibole. Fayalite occurs as both phenocrysts (021) and groundmass (019 and 021). Amphibole, aenigmatite and ilmenite are limited to single samples: Euhedral aenigmatite is present as phenocrysts up to 400 μm (sample 055); a single amphibole crystal (023) was found in disequilibrium with the matrix; ilmenite is found in the only sample to contains any quartz (021) as rare spherulitic intergrowths with feldspar (<200 μm). Vesicles are present in two samples (19 and 55). Inclusions of clinopyroxene and apatite are occasionally found in the feldspars within the same two samples. Microlites are numerous and are aligned in flow-bands. Scoria and pumice samples, which, due to rapid quenching usually provide superior MI samples (e.g. Anderson and Brown 1993), were found to be largely aphyric or with rare crystals too small to be utilised. The obsidians show no obvious evidence of weathering, rehydration or other secondary alteration in hand sample. The major phases are alkali feldspar and Fe–augite, with alkali feldspar the most promising MI host; rare MI were also located in Fe–augite and fayalitic olivine. MIs are remarkably scarce within the Dabbahu rocks; sample 055 yielded the greatest number.

Analytical techniques

Whole rock

Whole rock major and trace elements were analysed by X-ray fluorescence (XRF) using a fused glass discs and pressed powder pellets, analysed by a PANalytical Axios-Advanced XRF spectrometer at Leicester University. Loss on ignition was performed in two stages at 750°C and 950°C in order to minimise alkali loss from these peralkaline rocks. Major element whole rock data are given in Table 1.

Microanalysis

The samples were crushed by hand, and individual crystals, fragments of obsidian and pumice matrix glass were hand-picked, mounted in resin and polished to expose the MI. Prior petrographic observation ensured all the feldspar grains mounted contained MI (Fig. 2). In dark host minerals (e.g. Fe–augite), the mineral colouration concealed any inclusions, and these were therefore mounted en masse to maximise the opportunity of locating MI. Exposed MI were examined and mapped (uncoated to minimise carbon contamination) using a Hitachi S-3500N scanning electron microscope (SEM) at Bristol University. Any MI displaying cracks, re-entrants or obvious signs of post-entrapment processes were rejected. The 71 MI (59 in feldspar, nine in cpx, three in olivine), 12 obsidian matrix glasses and eight pumice matrix glasses were analysed by secondary ion mass spectrometry (SIMS) for dissolved H_2O and CO_2 and a number of trace elements, using a CAMECA ims-4f ion microprobe at the NERC facility, University of Edinburgh. To enhance relief, grain mounts were polished with 0.3 μm alumina for 30 s prior to gold coating. A 5 nA, 10 kV (nominal) O-beam with a 15 μm focused spot was used. Secondary ions were collected at 4.5 kV with a 75 eV offset to minimise molecular ion transmission. Samples were pre-sputtered using a 50 μm beam for 2 min to remove any surface contamination. Heavy and light trace elements were determined in two separate runs on exactly the same spot. NIST-28, NIST-610, RB-480, SISS-51 silica-rich glass standards, together with a rhyolite glass from Dabbahu as a monitor of background consistency were analysed at the start and end of each day. ^{12}C counts were corrected for the $^{24}Mg^{2+}$ isobaric interference by peak-stripping using $^{25}Mg^{2+}$ at mass 12.5 (Blundy and Cashman 2008). Because of the very low MgO contents of the studied glasses (<0.25 wt.%), the interference of $^{24}Mg^{2+}$ at ^{12}C is small. Uncertainties in element abundance, determined by normal error propagation, are <0.3 wt.% for all H_2O analyses (typically <0.01 wt.%) and <40 ppm for CO_2.

A CAMECA SX-100 electron microprobe at the University of Bristol was used for major element analysis. A 15 kV accelerating voltage, 4 nA beam current and defocused 10 μm beam was used for MI, matrix glasses and feldspar hosts, with Na analysed first to reduce the effects of alkali migration (Humphreys et al. 2006). For cpx and olivine hosts, a 20 kV accelerating voltage, 10 nA beam current and 1 μm beam was used. P, S and Cl were also analysed,

Table 1 Whole rock data for melt inclusion host samples and representative obsidians and pumices

Whole rock[a]	Melt inclusion host samples				Additional samples									
Sample	019	021	023	055	003	012	015	016	022	029	036	038	057	062
Type[b]	Rhyolitic obsidian	Rhyolitic obsidian	Rhyolitic obsidian	Rhyolitic obsidian	Pumice	Pumice	Rhyolitic obsidian	Rhyolitic obsidian	Rhyolitic obsidian	Rhyolitic obsidian	Pumice	Pumice	Rhyolitic obsidian	Pumice
	Pantellerite	Pantellerite	Pantellerite	Pantellerite	Pantellerite	Pantellerite	Pantellerite	Pantellerite	Pantellerite	Comendite	Comendite	Comendite	Pantellerite	Pantellerite
n	1	1	1	1	1	1	1	1	1	1	1	1	1	1
SiO_2	73.30	72.91	72.58	72.75	71.98	68.57	72.39	72.23	71.24	70.00	73.38	73.98	72.85	71.16
TiO_2	0.36	0.35	0.35	0.36	0.37	0.45	0.36	0.35	0.37	0.40	0.17	0.16	0.36	0.37
Al_2O_3	9.77	9.71	9.63	9.32	9.33	9.50	9.37	9.22	9.27	12.10	11.55	11.63	9.45	9.29
Fe_2O_3t	6.46	6.45	6.41	6.60	6.55	6.43	6.58	6.46	6.53	5.69	2.98	3.01	6.63	6.53
MnO	0.21	0.21	0.20	0.21	0.21	0.19	0.22	0.21	0.21	0.18	0.09	0.09	0.22	0.20
MgO	b.d.	b.d.	b.d.	b.d.	b.d.	b.d.	b.d.	b.d.	b.d.	b.d.	b.d.	b.d.	b.d.	b.d.
CaO	0.29	0.28	0.26	0.27	0.32	0.87	0.27	0.43	0.37	0.67	0.41	0.30	0.26	0.62
Na_2O	5.96	6.01	6.01	5.99	6.01	5.29	6.50	5.69	6.70	6.20	5.44	5.27	5.96	5.64
K_2O	4.17	4.30	4.40	4.25	4.38	4.25	4.44	3.24	4.18	4.48	4.40	4.43	4.18	4.09
P_2O_5	0.01	0.01	0.01	0.01	0.01	0.03	0.01	0.01	0.02	0.02	b.d.	b.d.	0.01	0.01
SO_3	0.02	0.02	0.01	b.d.	0.04	0.04	0.04	0.01	0.04	0.07	b.d.	0.02	b.d.	0.01
LOI	0.30	0.21	0.30	0.16	1.02	3.63	0.28	2.31	1.18	0.60	1.11	1.11	0.18	2.56
Total	100.85	100.46	100.16	99.92	100.21	99.27	100.45	100.09	100.11	100.39	99.94	100.00	100.09	100.46
mol (Na + K)/Al	1.5	1.5	1.5	1.5	1.6	1.4	1.7	1.4	1.7	1.2	1.2	1.2	1.5	1.5

[a] Major element analysis—XRF

[b] Rock type—definition based on total alkalis vs silica plot (TAS) and the comendite–pantellerite definition of MacDonald (1974), mol $(Na_2O+K_2O)/Al_2O_3>1$ is a definition of peralkalinity

n denotes number of analyses, *b.d.* below detection level, *n.c.* not calculated, *host* refers to phenocryst hosting the inclusion, *blank space* indicates no analysis

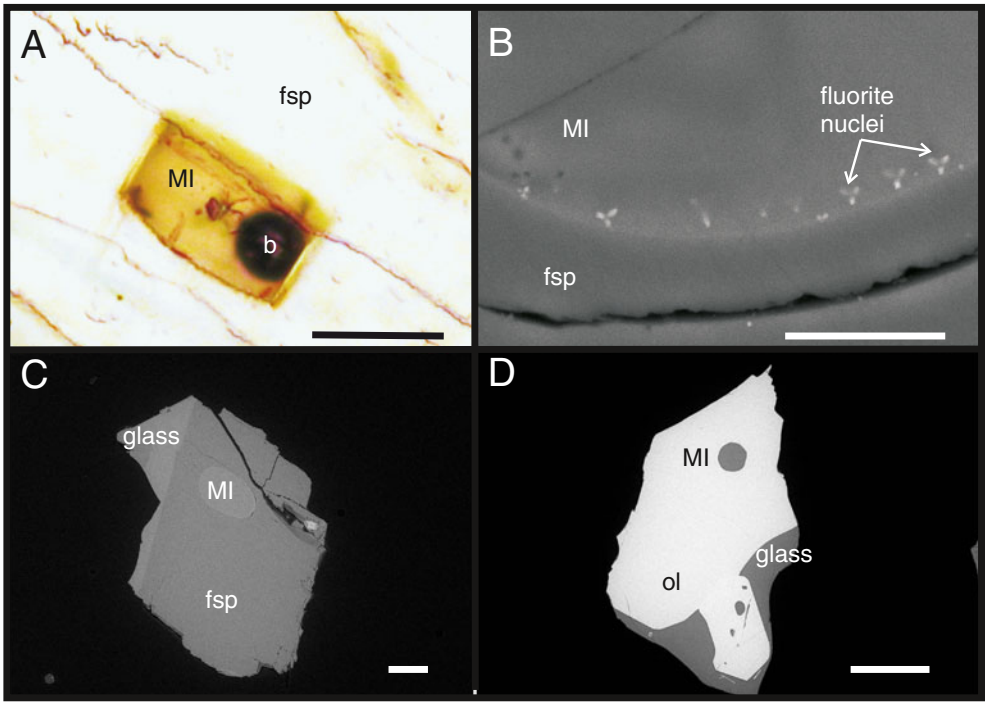

Fig. 2 Images of typical melt inclusions. **a** Photomicrograph of MI in feldspar (*fsp*) with bubble (*b*). Scale *bar* 20 μm. **b** BSE image of the MI used for element mapping showing fluorite nuclei around the MI rim, scale *bar* 10 μm. **c** BSE image of a MI in a feldspar host (sample 055). Scale *bar* in **c** and **d** 100 μm. **d** BSE image of a MI in olivine (*ol*) (sample 021)

with Zr in a subset of samples. Major, trace and volatile element analyses are given in Tables 2 and 4.

In order to assess the extent of chemical heterogeneity and minute daughter minerals, energy-dispersive element mapping was carried out on a typical MI from sample 055 (Fig. 2b) using the Hitachi S-3500N SEM with 40,000 cps, 20 kV with a dead time of ~30%, over an area ~40×30 μm. This procedure causes extensive damage to the MI rendering them unusable for further analysis and was therefore limited to a single inclusion.

Mid-IR spectra for H_2O in three matrix glasses were obtained using a Nicolet Nexus 670 FTIR spectrometer with an IR PLAN microscope attachment, Globar source, KBr beamsplitter and MCT detector (512 scans at 8 cm^{-1} resolution). Double- polished plates of around 80–380 μm thickness were prepared and measured with Mitutoyo Digital Micrometer to ±1μm. Samples were sectioned perpendicular to any flow banding to examine any variation associated with this feature. Absorption peak heights at 3,550 cm^{-1} were converted to concentrations using the Beer–Lambert equation and extinction coefficients of 56 L/mol cm (Newman et al. 1986). A density of 2,350 g/l was assumed (corrected to low pressure from Tamic et al. 2001).

Results

Whole rocks and matrix and pumice glasses

Major element data were assessed for post-eruptive alkali loss (e.g. through weathering) using the molar FK/Al (mol Fe + K/Al) vs NK/A (mol Na + K/Al) criteria of White et al. (2003). All samples used fell inside the 95% confidence lines consistent with a lack of any significant alkali loss. Samples 019, 021, 023 and 055 are peralkaline with a molar NK/A range from 1.5 to 1.6 and contain SiO_2 (anhydrous) whole rock contents of 73.1–73.4 wt.%. A direct comparison of matrix glasses from these samples show they are comparable; sample 021 contains rare quartz and feldspar spherules and has −0.6 wt.% lower SiO_2 (Tables 1 and 2). Other obsidian glasses and pumices samples show whole rock SiO_2 contents of 70.5–75.0 wt.% and matrix glass values of 72.1–75.3 wt.%. The H_2O content is low in obsidian matrix glasses <0.2 wt.%, consistent with extensive syn-eruptive degassing. Pumices have a higher range (0.2–1.2 wt.%), and it is possible that those pumices with higher water content may have suffered some minor secondary hydration and associated alkali loss. Likewise, CO_2 values range from below detection to <30 ppm in obsidian matrix glasses and <350 ppm in pumice glasses.

Alkali feldspar-hosted MI

The euhedral alkali feldspar hosts (<1 mm) are An-poor anorthoclase (AN_0) (Table 3, Fig. 3). In the rare instances MI were found, the host crystals typically contain a green (sample 055), to colourless (sample 019), single rounded or elongate MI up to ~150 μm in length. The primary concern when using MI to infer pre-eruptive volatile contents is whether they truly represent the original melt from which they were trapped, or whether post-entrapment modification has compromised them (Metrich and Wallace 2008). This

Table 2 Major and trace element analyses for obsidian matrix glasses and pumice matrix glasses

Sample	Pumice matrix glasses						Obsidian matrix glasses							
	003	012	022	036	038	062	015	016	019	021	023	029	055	057
n	2	8	2	2	2	2	12	12	19	12	12	11	14	12
$SiO_{2\ (wt\%)}$[a]	73.07	71.70	73.12	74.05	74.61	72.00	71.91	72.25	72.28	71.42	72.38	70.85	72.19	72.40
TiO_2	0.35	0.09	0.37	0.13	0.13	0.38	0.23	0.21	0.29	0.18	0.25	0.41	0.17	0.24
Al_2O_3	9.51	11.31	9.34	11.79	12.13	9.41	9.12	9.05	9.28	10.20	9.27	10.32	9.58	9.03
FeOt	5.96	3.13	6.19	2.51	2.41	5.96	6.12	6.01	6.03	5.51	5.88	5.65	5.72	5.95
MnO	b.d.	b.d.	b.d.	b.d.	b.d.	b.d.	0.19	0.15	0.22	0.16	0.22	0.13	0.16	0.17
MgO	0.21	0.06	0.25	0.06	b.d.	0.18	b.d.	b.d.	b.d.	b.d.	b.d.	b.d.	b.d.	b.d.
CaO	0.29	0.08	0.19	0.19	0.14	0.30	0.27	0.16	0.27	0.20	0.15	0.32	0.14	0.13
Na_2O	5.84	5.14	5.74	5.06	5.10	5.47	5.74	5.79	5.67	5.73	5.70	5.74	5.97	5.71
K_2O	4.38	4.44	4.42	4.57	4.39	4.39	4.32	4.33	4.32	4.50	4.31	4.48	4.43	4.31
ZrO						b.d.	0.06	0.02	0.10	0.11	0.05	0.06	0.05	0.03
P_2O_5	b.d.	b.d.	b.d.	b.d.	b.d.	b.d.	b.d.	b.d.	b.d.	b.d.	b.d.	b.d.	b.d.	b.d.
SO_2	b.d.	b.d.	b.d.	b.d.	b.d.	b.d.	b.d.	b.d.	b.d.	b.d.	b.d.	b.d.	b.d.	b.d.
F							0.24	0.25	0.24	0.25	0.25	0.26	0.23	0.27
Cl	0.2	0.05	0.21	0.19	0.21	0.19	0.09	0.10	0.13	0.09	0.10	0.10	0.12	0.10
Total	99.81	96.00	99.83	98.55	99.12	98.28	98.30	98.33	98.85	98.35	98.55	98.32	98.76	98.35
mol (Na + K)/Al[b]	1.5	1.2	1.5	1.1	1.1	1.5	1.5	1.6	1.5	1.4	1.5	1.4	1.5	1.6
n	1	1	1	1	1	1	1	1	1			1		1
H_2O (wt.%)[c]	0.19	1.18	0.32	1.19	0.81	0.16	0.16	0.16	0.16			0.16		0.22
Error[d]	0.003	0.009	0.006	0.013	0.005	0.003	0.013	0.003	0.0041			0.002		0.003
H_2O (wt.%)[e]									0.182 (6)		0.177 (6)		0.187 (9)	
error[f]									0.08		0.01		0.01	
CO_2 (ppm)[c]	44	98	35	70	b.d.	349	15	3	13			20	9	9
error[d]	13	23	20	16		24	7	5	6			12	11	10
T (°C) - ave[g]	n.c.	782	n.c.	n.c.	n.c.	n.c.	n.c.	n.c.	n.c.	n.c.	n.c.	n.c.	701	n.c.
P (Mpa)	n.c.	n.c.	n.c.	n.c.	n.c.	n.c.	n.c.	n.c.	n.c.	n.c.	n.c.	n.c.	n.c.	n.c.
Depth - ave	n.c.	n.c.	n.c.	n.c.	n.c.	n.c.	n.c.	n.c.	n.c.	n.c.	n.c.	n.c.	n.c.	n.c.
Li (ppm)[c]	40	37	40	40	41	37	39	38	40			34	39	42
Be	9.2	9.1	9.1	9.3	9.6	9.1	9.1	9.0	9.1			8.3	9.2	9.6
B	11	10	11	12	12	11	11	11	11			10	11	11
Sc	3.6	3.9	3.8	3.4	3.5	3.1	3.6	3.5	3.4			3.5	3.5	3.2
Rb	116	112	128	112	104	114	120	119	118			100	122	118
Sr	1.2	1.2	1.1	1.7	1.8	1.2	1.0	0.9	1.0			16.2	0.9	1.0

Table 2 (continued)

Sample	Pumice matrix glasses						Obsidian matrix glasses							
	003	012	022	036	038	062	015	016	019	021	023	029	055	057
Y	102	99	108	97	103	98	102	101	100			86	104	100
Zr	1087	1031	1161	824	823	1057	1093	1088	1070			937	1122	1072
Nb	170	155	182	129	126	166	171	172	165			141	176	165
Ba	14	14	15	85	88	14	14	14	16			302	13	13
La	107	104	114	63	67	103	108	106	103			95	110	105
Ce	213	207	229	134	149	208	216	215	208			192	217	206
Pr	25.3	24.0	26.5	15.7	18.1	25.0	25.3	25.8	24.8			21.9	26.0	24.8
Nd	109	107	117	69	82	101	109	107	106			99	111	103
Sm	21.3	21.9	22.2	14.6	17.6	20.6	21.3	21.7	21.4			17.9	22.1	21.1
Eu	2.8	2.9	2.9	1.9	2.2	2.7	2.6	2.8	2.8			4.9	2.8	2.9
Gd	30.1	28.9	29.9	18.4	19.1	25.8	26.4	28.2	25.3			24.8	28.9	28.1
Tb	4.2	4.1	4.4	3.1	3.7	4.2	4.0	4.3	3.8			3.4	4.2	4.2
Dy	32.6	31.4	35.2	25.2	29.2	31.1	33.8	34.5	31.5			28.1	32.7	31.8
Ho	4.3	4.2	4.7	4.1	4.3	4.2	4.2	4.5	4.2			3.9	4.6	4.1
Er	14.0	12.5	14.0	12.2	13.7	13.0	12.9	13.2	13.2			11.8	13.2	13.3
Yb	12.4	11.8	14.2	12.9	13.4	11.9	12.1	12.0	11.7			9.3	13.6	11.6
Lu	1.9	1.6	1.8	1.7	2.0	1.8	2.0	2.0	1.8			1.5	2.0	1.7
Hf	26	22	26	23	25	24	26	25	26			21	28	24
Ta	13	11	14	10	11	12	13	13	12			10	13	12
Th	11	9	11	11	11	10	10	11	10			9	11	10
U	3	3	3	3	3	3	3	3	3			3	3	3

[a] major element analysis - EMPA

[b] mol $(Na_2O + K_2O)/Al_2O_3 > 1$ is a definition of peralkalinity

[c] Secondary ion mass spectrometry (SIMS) analysis

[d] Average error as determined by full propagation of counting statistics, instrument background and calibration working curve

[e] Averaged matrix glass measured using FTIR analysis. Number in parenthesis is the number of measurements

[f] - Standard deviation

[g] -Temperature in °C using the method of (a) Putirka (2008) and (b). Calibration error ±23°C

n - denotes number of analyses, *b.d.* below detection level, *n.c.* not calculated

Blank space indicates no analysis

Table 3 Representative analyses of melt inclusion host crystals

Feldspar											CPX				Olivine		
Sample	019 fsp	019 fsp	021 fsp	021 fsp	023 fsp	023 fsp	023 fsp	055 fsp	55 fsp	55 fsp	Sample	055 cpx	055 cpx	055 cpx	Sample	021 ol	021 ol
SiO_2 (wt%)[a]	67.56	67.74	67.48	67.05	67.27	66.88	67.00	67.10	67.50	68.40	SiO_2	48.32	48.88	48.51	SiO_2	29.54	29.31
TiO_2	b.d.	b.d.	b.d.	b.d.	b.d.	b.d.	b.d.	b.d.	b.d.	b.d.	TiO_2	0.42	0.40	0.41	TiO_2	b.d.	0.03
Al_2O_3	18.28	18.53	18.38	18.85	18.71	18.76	18.26	18.13	18.14	18.77	Al_2O_3	0.17	0.15	0.17	Al_2O_3	b.d.	b.d.
FeOt	0.66	0.68	0.68	0.36	0.67	0.41	0.58	0.71	0.76	0.71	FeOt	30.96	31.33	31.02	FeOt	67.57	67.61
MnO	b.d.	b.d.	b.d.	b.d.	b.d.	b.d.	b.d.	b.d.	b.d.	b.d.	MnO	1.47	1.49	1.53	MnO	3.69	3.68
MgO	b.d.	0.07	b.d.	b.d.	b.d.	b.d.	b.d.	b.d.	b.d.	b.d.	MgO	0.11	0.08	0.07	MgO	0.07	0.08
CaO	b.d.	b.d.	b.d.	b.d.	b.d.	b.d.	b.d.	b.d.	b.d.	b.d.	CaO	17.14	16.65	16.81	CaO	0.46	0.50
Na_2O	8.04	8.04	7.78	7.92	7.83	8.03	7.94	7.33	7.92	7.63	Na_2O	2.01	2.35	2.06	Na_2O	b.d.	b.d.
K_2O	5.41	5.35	5.34	5.65	5.70	5.54	5.53	6.23	5.57	5.58	K_2O	b.d.	b.d.	b.d.	K_2O	b.d.	b.d.
P_2O_5					b.d.	b.d.	b.d.	b.d.			Cr_2O_3	b.d.	b.d.	b.d.	Cr_2O_3	b.d.	b.d.
SO_2	b.d.	b.d.	b.d.	b.d.	b.d.	b.d.	b.d.	b.d.	b.d.	b.d.	NiO	b.d.	b.d.	b.d.	NiO	b.d.	b.d.
Cl					b.d.	b.d.	b.d.	b.d.			ZnO	b.d.	b.d.	b.d.	ZnO	0.12	0.12
Total	99.95	100.41	99.66	99.83	100.18	99.62	99.31	99.50	99.89	101.09	Total	100.60	101.32	100.58	Total	101.45	101.33
An	0.0	0.0	0.0	0.0	0.0	0.0	0.0	0.0	0.0	0.0	Fe^{2+} [b]	0.20	0.22	0.18	Fo	0.2	0.2
Ab	69.3	69.5	68.9	68.1	67.60	68.8	68.60	67.8	67.0	67.1	Fe^{3+} [b]	0.86	0.84	0.87	Fa	99.8	99.8
Or	30.7	30.5	31.1	31.9	32.40	31.2	31.40	32.2	33.0	32.9	(Mg) En	0.4	0.3	0.2	Mg#	0.2	0.2
Si + Al + Ti + Fe	4.0	4.0	4.0	4.0	4.0	4.0	4.0	4.0	4.0	4.0	(Fe) Fs	58.3	59.3	58.9			
Ca + Na + K	1.0	1.0	1.0	1.0	1.0	1.0	1.0	1.0	1.0	1.0	(Ca) Wo	41.3	40.4	40.9			
											Mg#	0.8	0.6	0.5			

[a] major element analysis - EMPA

[b] $Fe^{2+/3+}$ in cpx calculated according to the method of Schumacher (1991)

b.d. - below detection level

blank space indicates no analysis

Mg#=100Mg/(Mg + FeOt + Mn)

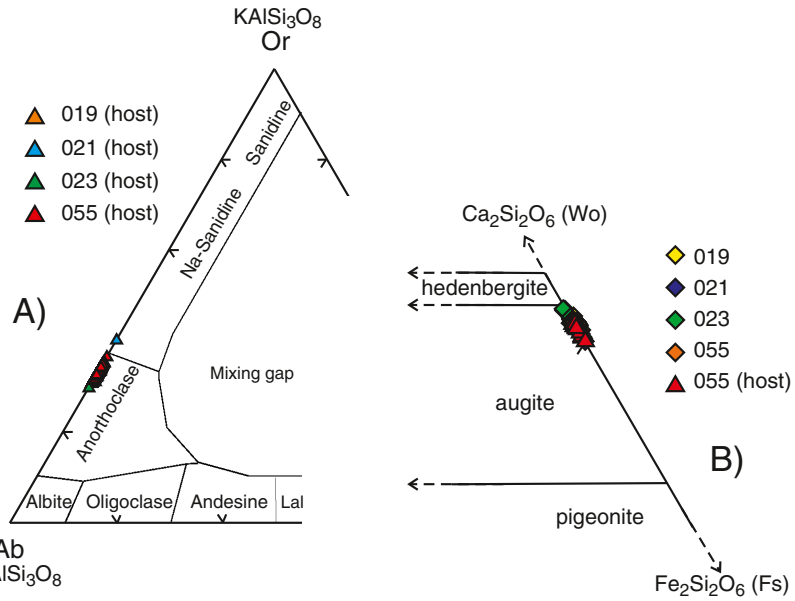

Fig. 3 Partial ternary classification diagrams for feldspar MI host crystals **a** and **b** pyroxene host (sample 055) and non-host compositions. Both *plots* show limited range in compositions

may be indicated by bubbles, devitrification, crystallisation or fracturing which can result in loss of vapour (Nielsen et al. 1998). All alkali feldspar hosted MI in this study contain one or more shrinkage bubbles up to 30 μm diameter, occupying an average of 2% of the total MI volume. Part of a typical MI was element mapped by SEM to check for signs of post-entrapment crystallisation; some nuclei (<1 μm) were visible under element mapping conditions at ~40,000 cps (Fig. 2b). The maps show these nuclei are CaF_2 indicating the inclusion was close to, or at, fluorite saturation. Phenocrystic fluorite has been found in Kenyan peralkaline rhyolites (Marshall et al. 1998) but has otherwise not been recorded in pantellerites, despite broadly similar fluorine contents.

The MI have values of molar NK/A of 1.1–1.8 that lie close to their host rocks (Tables 1 and 4), with SiO_2 content higher than the whole rock values (69.2–79.1 wt.%) on an anhydrous basis. H_2O content shows a wide range of 2.3 to 5.8 wt.%; CO_2 values vary from below detection to 462 ppm (Table 4: online resource 1 is a table containing all melt inclusion analyses).

Cpx- and olivine-hosted MI

Rare cpx-hosted MI were located in euhedral Fe–augites (sample 055), and where found, each contained one to two rounded MI. The crystals are <1 mm in length with average compositions of Wo_{41}, Fs_{58} and En_0 (Table 3, Fig. 3). The MI are up to ~150 μm in length (average ~71 μm). If present, bubbles are small, up to ~18 μm diameter. The largest bubble occupies 11% of the volume of the total MI, but the smaller bubbles average 1% volume. The MI have an SiO_2 range of 71.8–74.9 wt.%. H_2O contents lie at or below the low end of the alkali feldspar-hosted MI (1.1–3.6 wt.%), whereas CO_2 values (26–308 ppm, with one inclusion containing 1,457 ppm) extend the range to higher values (Table 4).

Three subhedral fayalite olivine hosts ($Fa_{99.7–100}$) (Table 3) were located in sample 021 each containing a single, bubble-free, MI <36 μm diameter. Typically olivine-hosted MI is corrected for post-entrapment crystallisation (Danyushevsky et al. 2000). However, due to the lack of MgO in both the MI and the host, this has not been possible. The MI have an SiO_2 range of 69.2–69.9 wt.% and low volatile contents: 0.2–0.6 wt.% H_2O and 279–484 ppm CO_2 (Table 4).

Comparison to volatile contents of other peralkaline rhyolites

Early studies of peralkaline rhyolites proposed that H_2O contents were low (<0.5 wt.%) based on low H_2O and high Cl concentrations within matrix glasses (Bailey et al. 1974; Bailey and Macdonald 1969; Nicholls and Carmichael 1969). MI studies have now been published from a range of peralkaline rhyolites, which consistently show relatively high H_2O contents, e.g. Pantelleria, Italy, 1.4–4.3 wt.% (e.g. Lowernstern and Mahood 1991; Gioncada and Landi 2010), Greater Olkaria Province, Kenya, 0.9–3.4 wt.% (5.7 wt.% after accounting for degassing; Wilding et al. 1993), Fantale, Ethiopia, 0.4–8.5 wt.% (mean of 4.6–4.9 wt.%) (Webster et al. 1993), Mayor Island, NZ, 2.6–5.0 wt.% (Barclay et al. 1996), Baitoushan Volcano, China/North Korea, 1.3–6.6 wt.% (Horn and Schmincke 2000). Experimental studies such as those from Pantelleria and Eburru, Kenya, which suggest peralkaline pre-eruptive water contents were >4 wt.%, even as high as 5–6 wt.%, support these findings (Di Carlo et al. 2010; Scaillet and Macdonald 2001, 2006).

Table 4 Major and trace element analyses for representative melt inclusions

Sample	019 a	019 b	021 a	021 b	023 a	023 b	21 d	21 e	055 a	055 c	055 i	055 a	055 c	055 h	055 i	055 m	055 n	055 p	055 q	055 aa	055 ae	055 al
host	fsp	fsp	fsp	fsp	fsp	fsp	ol	ol	cpx	cpx	cpx	fsp	fsp	fsp	fsp	fsp	fsp	fsp	fsp	fsp	fsp	fsp
Type[a]	p	p	p	p	p	p	p	p	p	p	p	p	p	p	p	p	p	p	p	p	p	p
n	1	1	3	3	2	1	3	2	1	2	2	2	3	3	2	3	2	2	3	3	2	2
SiO_2 (wt.%) [b]	71.51	72.43	70.45	70.40	75.31	72.85	69.92	69.40	74.90	71.82	72.68	71.02	70.66	71.35	71.50	70.07	71.07	71.11	70.69	70.12	70.10	72.56
TiO_2	0.29	0.29	0.45	0.47	0.46	0.49	0.54	0.38	b.d.	0.39	0.44	0.45	0.51	0.51	b.d.	0.50	0.55	0.47	0.50	0.26	0.45	0.61
Al_2O_3	9.46	9.19	8.23	8.32	6.38	6.28	12.28	12.44	10.65	9.54	9.51	8.23	8.84	7.86	8.35	8.06	8.07	8.14	8.16	10.07	8.93	6.79
FeO	5.10	5.06	4.91	5.07	4.89	5.25	6.31	5.94	3.53	3.95	4.31	5.59	5.49	6.08	5.46	6.18	5.86	4.98	5.76	4.95	5.16	6.42
MnO	0.18	0.19	0.19	0.16	0.28	0.26	0.24	0.21	b.d.	b.d.	0.19	0.27	0.21	0.29	0.26	0.23	0.27	0.22	0.23	0.18	0.23	0.35
MgO	b.d.	b.d.	b.d.	b.d.	b.d.	b.d.	b.d.	b.d.	b.d.	b.d.	b.d.	b.d.	b.d.	b.d.	b.d.	b.d.	b.d.	b.d.	b.d.	b.d.	b.d.	b.d.
CaO	0.18	0.16	0.12	0.22	b.d.	b.d.	0.43	0.48	0.13	0.15	0.28	0.17	0.26	0.26	0.19	0.35	0.23	0.15	0.20	0.42	0.18	0.11
Na_2O	5.48	5.42	4.90	5.13	4.49	4.43	6.15	6.10	3.96	4.55	5.27	5.26	5.30	5.18	5.19	5.37	5.05	5.12	5.31	6.12	5.77	2.87
K_2O	4.23	4.28	4.06	4.06	3.37	3.60	4.87	4.80	4.67	4.69	4.64	4.16	4.15	4.06	4.21	4.09	4.14	4.24	4.17	4.46	4.16	3.68
P_2O_5	b.d.	b.d.	b.d.	b.d.	b.d.	b.d.	b.d.	b.d.	b.d.	b.d.	b.d.	b.d.	b.d.	b.d.	b.d.	b.d.	b.d.	b.d.	b.d.	b.d.	b.d.	b.d.
SO2	b.d.	b.d.	0.04	b.d.	b.d.	b.d.	0.04	0.06	b.d.	0.06	b.d.	0.05	0.05	b.d.	0.05	0.07	0.04	0.05	0.05	b.d.	b.d.	0.06
ZrO			0.25	0.24			0.21	0.25	b.d.	0.22	b.d.	0.23	0.24	0.34	b.d.	b.d.	0.2	0.35	0.4	b.d.	b.d.	
Cl	0.23	0.27	b.d.	0.25	0.30	0.30	0.21	0.2	0.2	0.19	0.22	0.26	0.22	0.25	0.25	0.27	0.27	0.25	0.24	0.15	0.21	0.31
F															0.30		0.18					
Total	96.43	97.02	93.60	94.07	95.18	93.16	100.99	100.06	97.84	95.37	97.32	95.43	95.71	95.93	95.21	94.92	95.48	94.83	95.47	96.58	94.98	93.45
mol (Na + K)/Al[c]	1.5	1.5	1.5	1.5	1.7	1.8	1.3	1.2	1.1	1.3	1.4	1.6	1.5	1.6	1.6	1.6	1.6	1.6	1.6	1.5	1.6	1.3
n	1	1	1	1	1	1	1	1	1	1	1	1	1	1	1	1	1	1	1	1	1	1
H_2O (wt.%)[d]	3.38	2.29	5.79	5.57	3.96	5.25	0.28	0.57	3.24	3.56	3.27	3.91	4.21	4.55	4.03	3.98	3.59	3.38	3.55	3.48	4.50	3.94
Error[e]	0.02	0.04	0.09	0.11	0.03	0.006	0.004	0.009	0.097	0.08	0.08	0.032	0.030	0.049	0.040	0.057	0.047	0.058	0.059	0.050	0.097	0.25
CO_2 (ppm)[d]	52	89	32	71	157	76	279	484	280	1457	44	49	138	34	25	8	96	9	9	30	9	317
Error[e]	38	24	25	15	18	12	21	34	6	34	1	5	8	18	12	13	19	10	11	13	17	42
T (°C)	746	744	738	764	699	711	n.c.	n.c.	n.c.	800[e]	n.c.	755	772	781	760	803	776	754	766	807	745	789
P (MPa)	74	43	180	178	103	155	n.c.	n.c.	n.c.	284	n.c.	95	123	126	98	99	92	69	77	82	114	141
Depth	2.7	1.6	6.6	6.5	3.8	5.6	n.c.	n.c.	n.c.	16.0	n.c.	2.4	4.1	4.6	3.6	3.6	3.3	2.5	2.8	3.0	4.2	5.1
Li (ppm)[d]	39	41	51	35	40	35	20	20		36	33	48	45	51	50	46	45	42	46	52	51	71
Be	8.8	8.8	9.1	8.0	8.3	8.2	6.8	8.9		7.4	9.1	9.1	9.1	9.7	9.2	8.9	8.9	8.4	9.0	8.8	8.9	12.6
B	12	12	13	11	15	15	8	10		10	12	12	12	13	12	12	12	12	12	13	13	14
Sc	6.4	3.6	4.0	3.8	4.4	3.9	3.8	3.6		6.3	4.0	3.5	3.8	4.2	3.5	4.0	3.8	3.9	4.0	3.9	3.8	1.2
Rb	151	161	185	176	203	199	113	108		124	140	154	153	154	167	163	166	159	162	175	178	142
Sr	0.9	1.0	0.7	0.9	0.8	0.6	5.3	5.4		2.4	1.0	0.8	0.9	0.9	1.1	0.8	1.0	1.7	1.1	0.7	0.6	1.3
Y	93	94	104	106	117	88	84	92		137	119	111	101	118	109	110	110	109	112	111	113	148
Zr	1043	1059	1173	1152	1220	1168	856	980		1221	1170	1226	1124	1239	1205	1193	1245	1228	1219	1326	1250	1728
Nb	157	169	190	198	226	186	128	147		179	197	199	180	203	205	211	213	210	208	211	213	280
Ba	15	14	16	16	13	12	285	288		16	15	18	19	17	19	13	15	30	17	19	12	13
La	100	103	115	119	125	92	88	103		135	129	121	113	130	120	127	123	123	127	126	127	169
Ce	203	212	237	244	259	189	175	201		331	274	249	235	266	255	264	254	257	265	262	267	352
Pr	23.8	24.6	27.8	28.1	30.4	22.0	20.3	23.4		43.6	32.4	30.0	26.5	31.7	30.1	30.7	29.6	29.1	30.4	30.8	30.9	40.3
Nd	103	106	115	121	132	95	87	100		196	145	125	114	133	121	132	124	127	126	127	133	166

Table 4 (continued)

Sample	019 a	019 b	021 a	021 b	023 a	023 b	21 d	21 e	055 a	055 c	055 i	055 a	055 c	055 h	055 i	055 m	055 n	055 p	055 q	055 aa	055 ae	055 al
host	fsp	fsp	fsp	fsp	fsp	fsp	ol	ol	cpx	cpx	cpx	fsp	fsp	fsp	fsp	fsp	fsp	fsp	fsp	fsp	fsp	fsp
Type[a]	p	p	p	p	p	p	p	p	p	p	p	p	p	p	p	p	p	p	p	p	p	p
Sm	19.0	20.8	22.1	24.3	23.6	17.9	16.6	17.6		37.4	28.6	23.0	22.0	23.7	22.1	22.9	23.9	22.8	23.9	24.5	23.2	32.3
Eu	2.4	2.6	2.7	2.9	3.4	2.2	5.4	5.7		5.0	3.3	3.1	2.8	3.4	2.9	3.1	3.1	3.6	3.2	3.3	3.4	5.3
Gd	24.9	24.4	35.3	35.9	30.4	20.7	30.5	34.5		51.7	45.0	30.1	37.1	45.0	36.5	41.1	39.7	41.4	38.3	40.7	43.5	21.7
Tb	3.9	4.0	4.9	5.0	4.7	3.1	3.7	4.2		8.1	5.5	5.4	5.4	5.5	5.4	5.8	6.1	5.7	5.6	5.1	5.7	5.6
Dy	30.7	30.7	27.5	28.5	36.5	28.8	22.7	23.6		40.1	29.6	27.8	26.8	30.6	28.7	32.1	31.2	31.5	32.3	29.5	30.3	45.3
Ho	4.1	3.9	4.3	4.7	5.1	3.7	3.8	4.4		6.5	5.3	4.8	4.5	5.3	4.8	5.2	5.3	5.4	5.3	5.3	5.2	6.6
Er	12.5	12.5	b.d.	b.d.	16.2	12.8	b.d.	b.d.		b.d.	b.d.	b.d.	b.d.	b.d.	b.d.	b.d.	b.d.	b.d.	b.d.	b.d.	b.d.	21.9
Yb	11.4	10.9	0.4	3.1	14.1	10.7	b.d.	b.d.		4.4	0.5	b.d.	b.d.	b.d.	1.2	b.d.	b.d.	b.d.	2.0	b.d.	b.d.	21.9
Lu	1.5	1.7	b.d.	b.d.	2.1	1.7	b.d.	b.d.		b.d.	b.d.	b.d.	b.d.	b.d.	b.d.	b.d.	b.d.	b.d.	b.d.	b.d.	b.d.	3.3
Hf	23	23	28	28	30	29	21	26		36	27	31	28	30	31	30	31	32	31	35	31	47
Ta	11	12	12	14	14	14	9	10		14	13	14	13	12	14	15	15	15	15	15	14	22
Th	10	11	11	11	13	12	8	9		11	12	12	10	11	12	12	12	13	12	13	12	19
U	3	3	3	3	4	4	2	2		3	3	3	3	3	4	4	4	4	3	4	3	6

[a] Comendite–pantellerite definition of (MacDonald 1974), *p* is pantellerite, *c* is comendite

[b] Major element analysis—EMPA

[c] mol $(Na_2O+K_2O)/Al_2O_3>1$ is a definition of peralkalinity

[d] SIMS analysis

[e] Average error as determined by full propagation of counting statistics, instrument background and calibration working curve

[f] Temperature could not be calculated. 800°C was used as a nominal temperature to allow for calculation of pressure

Host refers to phenocryst hosting the inclusion, *n* denotes number of analyses, *T* temperature in °C using the method of Putirka (2008), *calibration error* ±23°C, *P* pressure in megapascals using VolatileCalc (Newman and Lowenstern 2002), *D* depth calculated from *P* assuming a crustal density of ~2,800 kg m^{-3}, *b.d.* below detection level, *n.c.* not calculated, *blank space* indicates no analysis

Major and trace element systematics

Major element data for Dabbahu, as a whole, span a wide compositional range from basalt to rhyolite (Barberi et al. 1974a) consistent with protracted fractional crystallisation of basaltic parent magma. Here, we focus only on the intermediate and silicic rock types (>58 wt.% SiO_2), in order to provide a framework for interpreting the MI data. Whole-rock data in Table 1, for the samples studied here, are augmented by unpublished data for intermediate rocks. Whole rocks up to ~69 wt.% SiO_2 show a single magmatic lineage characterised by increasing K_2O, roughly constant Al_2O_3 and falling TiO_2 and FeO, although the latter shows some scatter (Fig. 4). Above 69 wt.%, SiO_2 the evolved rocks show two divergent trends, comendites (low FeO, high Al_2O_3) and pantellerites (high FeO, low Al_2O_3). Strong negative correlation between FeO and SiO_2 (Fig. 4a) in the comendites requires higher proportions of Fe–augite than in pantellerites. The modest fall in TiO_2 with SiO_2 for both suites (Fig. 4d) is consistent with the presence of accessory ilmenite.

Matrix glasses from pumices and obsidians lie at the high SiO_2 end of the corresponding whole rock trends for comendites and pantellerites, consistent with the nature of the host rock. The very limited enrichment of matrix glass SiO_2 compared with whole rocks is consistent with very low phenocryst contents. The MI span a wide range of SiO_2 (69–78 wt.%) that overlaps but extends the whole rock range. The olivine-hosted MI lie at the low SiO_2 end of the range, consistent with trapping at a relatively early stage of magma differentiation. The alkali-feldspar hosted inclusions provide the closest match to the whole rocks, but also extend to the highest SiO_2. Close agreement between the composition of the alkali feldspar-hosted inclusions and the

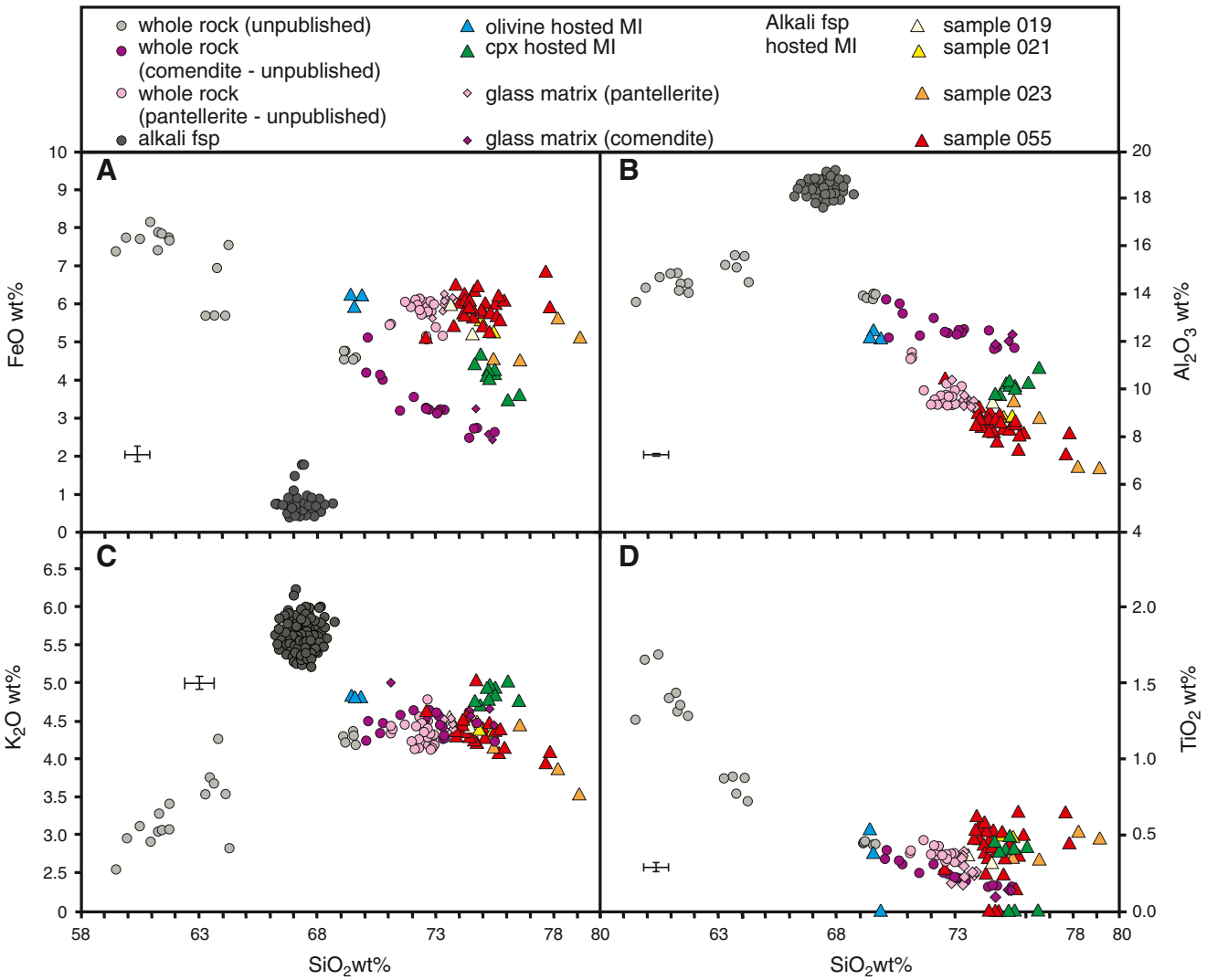

Fig. 4 Selected Harker diagrams for major element oxides (wt.% basis, normalised to 100% anhydrous). Data augmented by unpublished whole rock (XRF) data, and where applicable, alkali feldspar data. Typical uncertainties (1σ) indicated by error *bars*

whole rocks testify to limited post-entrapment crystallisation of the MI around their walls, consistent with our petrographic observations. However, there is scatter evident in the FeO–SiO_2 plot (Fig. 4a), which may be caused by crystallisation of alkali feldspar, which is low in FeO. Based simply on mass balance considerations, the amount of post-entrapment crystallisation is modest, about 10 wt.% in the case of the most FeO-rich MI. The majority of the inclusions do not form an array that back-projects to alkali feldspar compositions, best seen in the Al_2O_3–SiO_2 plot (Fig. 4b), instead extending the whole-rock trend, which is itself controlled by both alkali feldspar and mafic minerals, such as Fe–augite. Thus, post-entrapment crystallisation cannot be considered as the primary driver of MI compositional variation. The same cannot be said of the Fe–augite-hosted MI, which do not match the whole rock pantellerites having lower FeO and higher K_2O and Al_2O_3. We attribute these discrepancies to post-entrapment crystallisation of host Fe–augite with ~31 wt.% FeO (Table 3). Again, using mass balance constraints, the extent of post-entrapment crystallisation is only 7 wt.%. The offset is simply more pronounced than for alkali feldspar host MI because the host mineral is so different in composition to the MI. In summary, the amount of post-entrapment crystallisation suffered by the MI suite as a whole is sufficiently small that our measured MI volatile contents are likely to deviate from their true values at entrapment by no more than 10% relative and, in the vast majority of cases, much less. For that reason, we have not attempted to make any post-entrapment crystallisation corrections to volatile contents as measured.

Trace element concentrations in matrix and MI glasses also overlap with whole rock data, e.g. for Zr (Fig. 5a). The high Zr contents (>1,000 ppm) are a consequence of the high solubility of zircon in peralkaline melts; only the comendites show any evidence for a drop on Zr at high SiO_2, consistent with eventual zircon saturation. Zircon crystals are not observed in the samples considered in this paper, although zircon crystals have been identified in one comendite and one metaluminous rhyolite from Dabbahu. Pairs of incompatible trace elements, such as Nb and Zr (Fig. 5b) are strongly correlated and lie at the high concentration extrapolation of the trachyandesite and trachyte whole rocks and overlap with the comendites and pantellerites. Some comendites are displaced to slightly lower Nb at a given Zr, perhaps due to a greater role of ilmenite (which can accommodate Nb) in the evolution of these rocks. Again the olivine-hosted MI are the least evolved in terms of their incompatible trace elements. A single Zr-rich (1,720 ppm) alkali-feldspar hosted MI (055-al; Table 4) may have experienced significant post-entrapment crystallisation, although the FeO content (6.42 wt.%) is not remarkably high.

The wide range in Zr content and the demonstrable incompatibility of this element make it a useful monitor

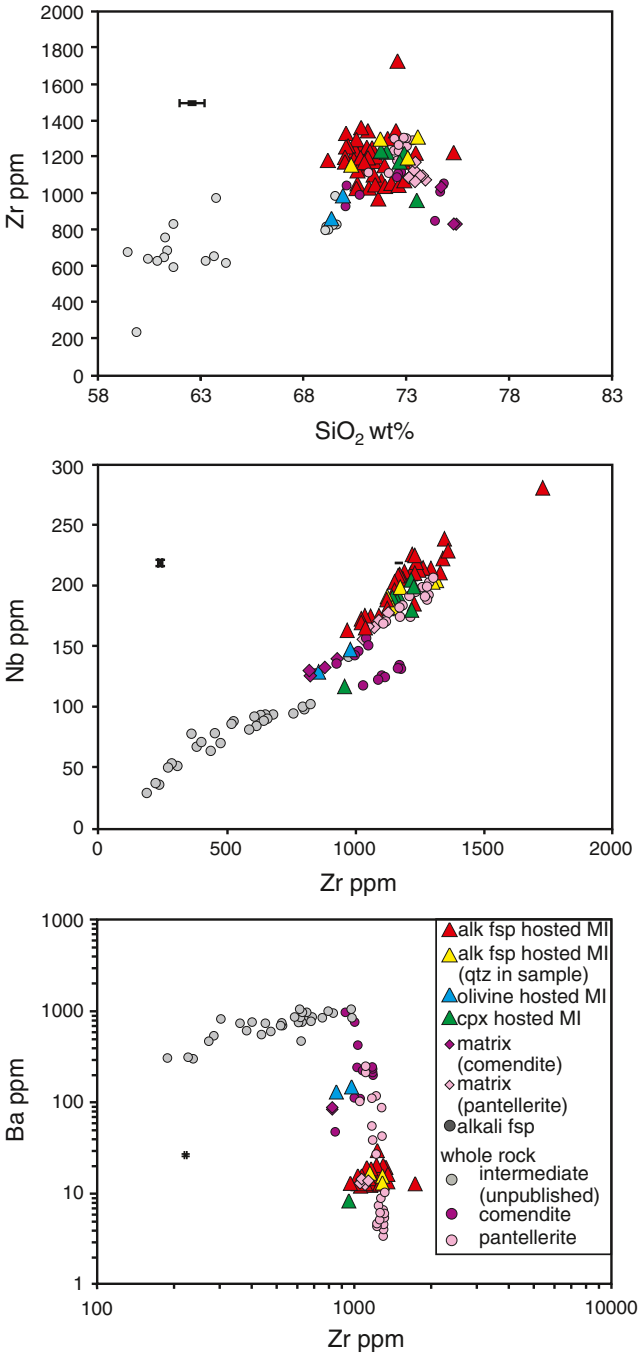

Fig. 5 Diagrams of Zr concentration in whole rock, MI and matrix glasses plotted against **a** SiO_2, **b** Nb, **c** Ba—note the logarithmic scale. Typical uncertainties (1 SD based on counting statistics) indicated by error *bars*

of the extent of fractionation (*F*). Zr is not well correlated with SiO_2 (Fig. 5a), indicating that the latter component does not adequately reflect F. Thus, the total change in *F* for MI, notwithstanding the anomalous high Zr sample, is a factor of 1.75, equivalent to 57% crystallisation, yet the total increase in SiO_2 over the same interval is only 69 to 75 wt.%. In a large part, this reflects the high SiO_2 content

of the alkali-feldspar-dominated crystallising assemblage, such that large amounts of crystallisation manifest as only small changes in SiO_2. The onset of alkali feldspar crystallisation is evident on a logarithmic plot of Ba (which is compatible in alkali feldspar) versus Zr (Fig. 5c). In summary, the chemical variation in the comendites and pantellerites reflects considerable fractionation, despite little variation in SiO_2. The lack of any significant correlation between an incompatible trace element, such as Zr, and SiO_2 (Fig. 5a) is suggestive of near-eutectic behaviour; the major elements are buffered within the system and therefore vary little during crystallisation. One explanation is that crystallisation took place close to the ternary minimum. In metaluminous systems, it is possible to use the composition of melts within the haplogranite system (orthoclase–albite–quartz) to establish eutectic behaviour and estimate the crystallisation pressure(s). The subaluminous, peralkaline nature of the rocks from Dabbahu removes them from the orthoclase–albite–quartz (Or–Ab–Qz) plane. Consequently, it is not possible to establish from their major elements alone if these melts are buffered in the Na_2O–K_2O–Al_2O_3–SiO_2 system. Thompson and Mackenzie (1967), inter alia, suggested that pantellerites lie within a 'low temperature zone' which had its origin in the 'thermal valley' of the granite system. The limited compositional range seen within anorthoclase phenocrysts from pantellerites was proposed by Thompson and Mackenzie (1967) as further evidence of the presence of a thermal valley, and this constancy of composition can be seen within the phenocrysts from Dabbahu, e.g. sample 055 with Ab 64–69 and Or 30–35 (Fig. 3). However, Macdonald et al. (2011) suggest that this low temperature zone may not apply to all peralkaline suites.

Volatile elements

Figure 6 is a conventional plot of CO_2 versus H_2O in the analysed matrix and MI glasses. As noted above, we have made no attempt to correct volatile contents for post-entrapment crystallisation, which we consider to have been minor. The bulk of the MI lie between 3 and 6 wt.% H_2O with CO_2 contents ≤400 ppm. The matrix glasses have less than 0.2 wt.% H_2O and, with a few exceptions, less than 80 ppm CO_2, consistent with extensive syn-eruptive degassing. All three olivine-hosted and a single cpx-hosted MI are displaced to very low H_2O (≤1 wt.%) from the main body of MI but at broadly similar CO_2 levels. The most ready explanation for these MI is that they have lost H_2O, either by diffusion through the host mineral or by leakage along cracks. The lack of evidence from major or trace elements for significant post-entrapment crystallisation suggests that diffusion loss was the primary cause of H_2O loss. Some groundmass glasses show elevated CO_2 and some interaction with CO_2-rich materials (magmatic vapours, sediments) cannot be ruled out. A single cpx-hosted MI lies at high CO_2 (1,457 ppm) and 3.5 wt.% H_2O. This is, by some margin, the most volatile-rich (and hence highest pressure) inclusion analysed. The field defined by the bulk of the MI does not match the predicted variation from degassing, under a simple closed or open system, but suggests the MI represent multiple magma bodies at multiple pressures, which are all undergoing vapour-saturated crystallisation (Blundy and Cashman 2008). In the presence of a mixed H_2O–CO_2 vapour, crystallisation of anhydrous phases drives the melt composition to high H_2O because of preferential loss of CO_2 to the vapour. In the simple isobaric case, the melt tracks along an isobar (shown as dotted lines in Fig. 6). This polybaric, vapour-saturated crystallisation, for example,

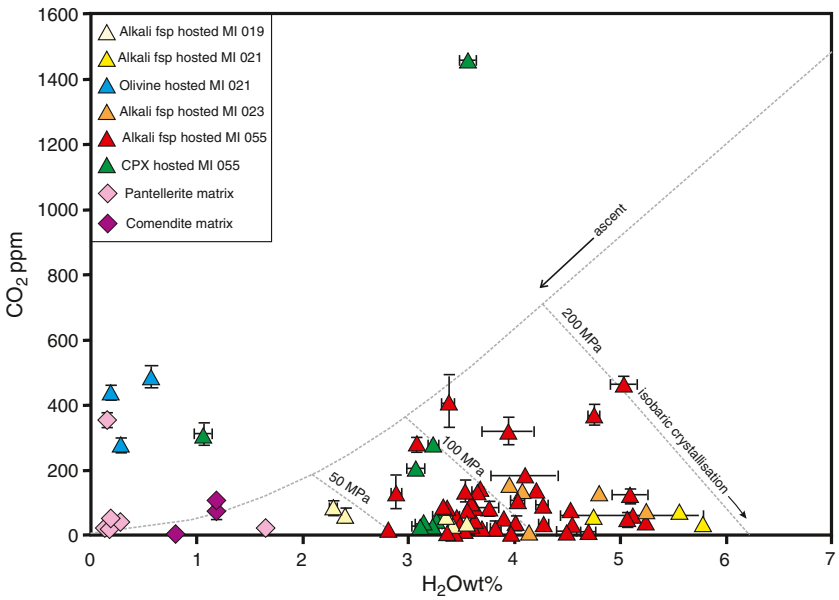

Fig. 6 MI and matrix glass volatile measurements on a conventional CO_2 versus H_2O plot. *Dotted lines* are isobars; *dashed line* denotes isopleth for 20 mol% H_2O in the vapour. Isobars and isopleths were calculated from VolatileCalc (Newman and Lowenstern 2002). Melts that stall at depth and undergo isobaric crystallisation follow the trend shown by the *arrow*. The olivine-hosted melt inclusions and a single low-H_2O cpx hosted melt inclusion appear to have lost H_2O

in a vertical extensive plumbing system, leads to displacement of the MI across several isobars, as observed. The greater the extent of crystallisation, the greater is the displacement to high H_2O. The data in Fig. 6 are consistent with the large amounts of crystallisation recorded by the MI, as deduced from trace element systematics.

We have insufficient data to constrain the volatile content of melt entering this shallow plumbing system. However, it is noteworthy that the CO_2-rich, cpx-hosted MI lies at the high-pressure end of a closed-system degassing trend that passes through the edge of the main MI data field, as shown by the dashed line labelled "ascent" in Fig. 6. Ascent of a volatile-saturated magma of this composition into a vertically extensive shallow system, covering a pressure range of ~50–200 MPa, followed by crystallisation will produce the observed MI field. Ascent and degassing of these magmas upon eruption will lead to loss of both H_2O and CO_2, yielding the observed matrix glass compositions. The data suggest that, unlike some silicic systems (e.g. Mount St. Helens; Blundy and Cashman 2005), decompression is not the main driving force behind crystallisation at Dabbahu. This is apparent from the lack of a negative correlation between incompatible trace elements, such as Zr (Fig. 7), and H_2O. Instead, we propose that crystallisation is driven primarily by cooling.

We have also measured Cl and F in a subset of MI and matrix glasses (Tables 2 and 4). Cl contents are remarkably constant at 0.25±0.03 wt.%, irrespective of whether glasses are inclusions or matrix. Evidently, degassing did not lead to Cl loss from the magma. Constant Cl is inconsistent with its behaviour as a truly incompatible element during crystallisation. Buffering of Cl contents will occur if the vapour phase is in equilibrium with a brine, as shown experimentally (Metrich and Rutherford 1992). We have not, however, observed any petrographic evidence for the presence of a coexisting brine phase. Fluorine contents, from six MI, are similar to Cl.

Magmatic temperatures

Calculating temperatures in peralkaline rocks is notoriously difficult due to the lack of suitable mineral assemblages. Many obsidian glasses and pumices are aphyric, and therefore temperatures cannot be calculated. Some success has been had with QUILF (e.g. White et al. 2005), but the host samples here lack the correct mineralogy. Temperatures reported here were calculated using the alkali feldspar-liquid thermometer of Putirka (2008). It was not possible to calculate temperatures for cpx- or olivine-hosted inclusions (using the relevant mineral thermometers), due to their very low MgO contents. Entrapment temperatures are within the range 696°C to 841°C (±23°C calibration uncertainty) for the alkali-feldspar-hosted MI samples (Tables 2 and 4). The maximum temperature range within samples (019 and 055) is 100°C ±23, (although sample 021 has just a 14°C range). The majority of the calculated temperatures cluster around 750°C which is comparable to temperatures found at Pantelleria for peralkaline samples (White et al. 2005). The large overall variation is likely to reflect temperature variations within the magma storage region, suggesting the temperature was not entirely homogenous, e.g. areas close to the chamber walls may have been cooler. If slow movement of the magma to the surface during eruption resulted in some cooling, MI trapped at this stage would indicate cooler entrapment temperatures. Cooling-induced, polybaric crystallisation is consistent with our interpretation of the MI data.

Magmatic pressures—constraints from experimental data

Constraints on magma storage conditions can be made using experimental studies on magmas with similar major element composition to those from Dabbahu. There have been no experimental studies of Dabbahu samples themselves,

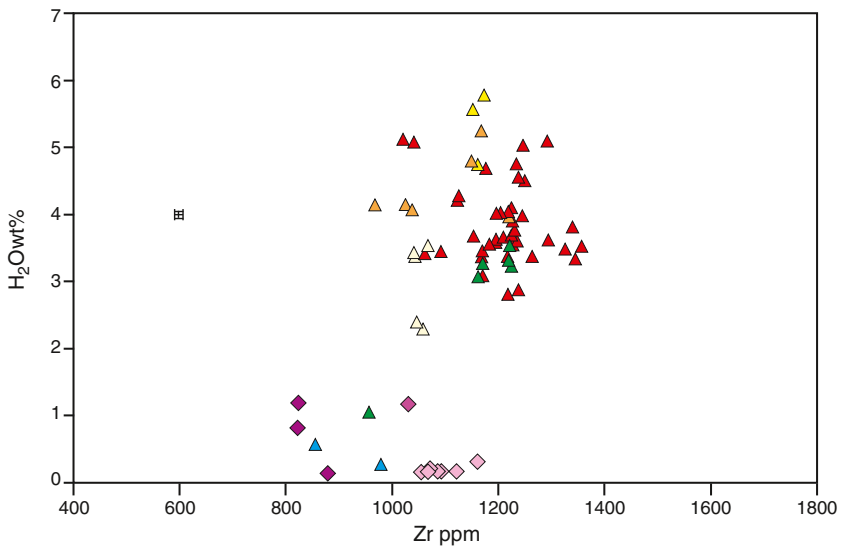

Fig. 7 Plot of H_2O vs. Zr, for MI and matrix glass measurements. The lack of correlation strongly suggests decompression crystallisation is not a strong factor in crystallisation at Dabbahu. Key same as for Fig. 6. Error *bars* indicate typical uncertainties

although Di Carlo et al. (2010) have determined the phase relations of a Pantelleria pantellerite (sample PAN 01113). Although Di Carlo et al. (2010) advise caution in using experimental data from one system to compare with another, their starting composition contained phenocrysts of alkali-feldspar, cpx and aenigmatite and had a similar bulk composition to the Dabbahu peralkaline rhyolites and therefore still provides a useful comparison. Di Carlo et al. (2010) determined phase relations in the presence of a mixed H_2O–CO_2 fluid, over a pressure range of 25 to 150 MPa, 680–800°C and fO_2 0.3 to 3.9 log units below the NNO buffer. Pressure, temperature and H_2O content are a strong influence on the equilibrium phase assemblage. It is therefore instructive to compare their experimentally determined phase relations to the phase assemblages at Dabbahu.

The phenocryst assemblage of 055 is alkali-feldspar + cpx + aenigmatite + apatite. The experiments of Di Carlo et al. (2010) show that the assemblage alkali-feldspar + cpx + aenigmatite is stable for H_2O-saturated conditions at 680°C and 100 MPa (4.1 wt.% H_2O in the melt) and for slightly H_2O-undersaturated conditions at 725°C and 150 MPa (2.7–3.4 wt.% H_2O in the melt). The presence of Ti-magnetite, as opposed to ilmenite, in most of their experiments likely reflects a small difference in fO_2, although a single H_2O-undersaturated run at 150 MPa, 750°C contains the assemblage alkali-feldspar + cpx + ilmenite + magnetite. Aenigmatite did not form in any experiment above 725°C, whereas amphibole (which is almost completely lacking at Dabbahu—just a single xenocryst in sample 023) was widespread for water under saturated conditions at temperatures below 700°C. However, it should be noted that many factors influence the presence of aenigmatite, and its presence alone cannot be used diagnostically (Macdonald et al. 2011). Finally, saturation in quartz (also rare at Dabbahu) occurs when water contents drop below 3.7 wt.% H_2O at 680°C and below ~1 wt.% at higher temperatures. Thus, based on these experiments alone, the field of stability of alkali-feldspar + cpx + aenigmatite ± ilmenite is 100–150 MPa and 680°C to 725°C for melt H_2O contents between 2.7 and 4.1 wt.%. These conditions overlap well with those that we have deduced from a combination of volatile solubility and alkali-feldspar thermometry and give us confidence in our petrological methods. Experimental mineral compositions also closely match those at Dabbahu. At 150 MPa and 725°C, the experimental alkali feldspar is Ab_{66}, which is identical to that in sample 055.

In summary, our calculated pre-eruptive storage conditions for sample 055 are consistent with the experimental data, in terms of pressure, temperature and H_2O content. The 055 magma was stored at or just below H_2O saturation, at temperatures of around 720–780°C and pressures of ~100 MPa. The experiments offer no higher pressure bound on this assemblage, although our MI data suggest that pressures can be significantly higher (up to 207 MPa).

Magmatic pressures—melt inclusions

In order to reconstruct confidently magma storage pressure from melt inclusions, petrological methods require various criteria to be fulfilled. MI should be volatile saturated and show no post-entrapment volatile leakage. The magmatic temperature estimate should be reliable, and the volatile solubility model should account for the peralkaline nature of the melts at Dabbahu.

If the melt was not saturated at the time of MI entrapment, the pressure calculated provides a minimum only. The pumice and glass matrices have largely degassed prior to quenching (Fig. 6), and small-volume bubbles in the alkali-feldspar-hosted MI suggests some loss of volatile content from melt into bubbles during quenching. Blundy and Cashman (2008) discuss the different evolutionary trends, in terms of dissolved H_2O and CO_2 that a melt can follow for different scenarios, such as isobaric volatile-saturated crystallisation, decompression crystallisation, volatile-undersaturated crystallisation, etc. The observed array of CO_2 and H_2O in the MI (Fig. 6) closely matches their predictions for vapour-saturated crystallisation over a range of pressure. Vapour-undersaturated crystallisation leads to simultaneous increase in both H_2O and CO_2, which is not observed in our data.

Loss of volatiles from a MI will also lead to pressure underestimates. On the basis of Fig. 6, we have argued that olivine-hosted MI and one cpx-hosted MI have lost H_2O, probably by diffusion, but that alkali feldspar MI volatiles are largely intact.

There is no reliable method for calculating saturation pressures in peralkaline rocks as H_2O and CO_2 solubility are known to have a strong compositional dependence on alkali content (e.g. Dixon 1997; Tamic et al. 2001). Both VolatileCalc (Newman and Lowenstern 2002) and the solubility model of Papale et al. (2006) significantly underestimate saturation pressures based on experiments (Fig. 8) from Di Carlo et al. (2010) and Scaillet and Macdonald (2003). We chose to use VolatileCalc (Newman and Lowenstern 2002) to calculate pressure from the CO_2 and H_2O data; on the basis of Fig. 8, these pressures should be seen as minima. The calculated entrapment pressure yields a range of 43–207 MPa, at temperatures of 679–841°C (average ~100 MPa). The single CO_2-rich cpx-hosted MI gives a pressure of 284 MPa for a nominal temperature of 800°C.

Magma storage depths

Having established that our pressure estimates are reasonable, pressure is converted into depth. The exact density structure beneath Dabbahu is unknown, and therefore a crustal density of

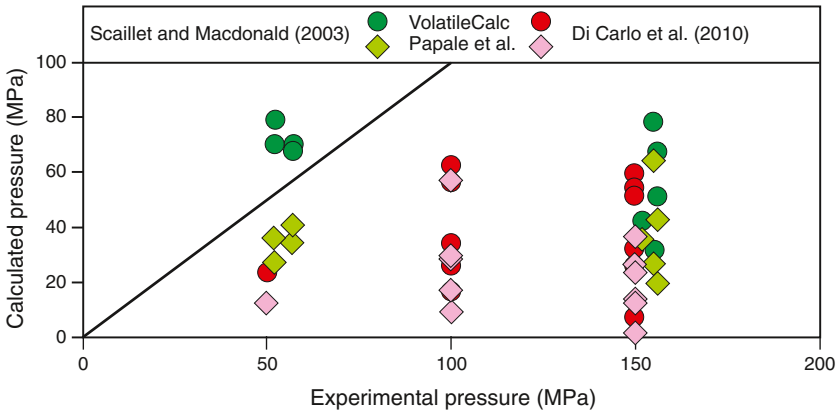

Fig. 8 Plot of calculated pressure using the models of Papale et al. (2006) and VolatileCalc (Newman and Lowenstern 2002) against experimental pressures from the studies of pantellerite rocks of Scaillet and Macdonald (2003) and Di Carlo et al. (2010). The *black line* shows a 1:1 correspondence. Note the underestimation of pressure by both models at pressures >50 MPa. Pressures were

2,800 kg m^{-3} has been assumed, based on regional gravity studies in the Ethiopian rift and in Southern Afar (e.g. Cornwell et al. 2006; Mahatsente et al. 1999; Mickus et al. 2007). The calculated pressures were used to calculate a depth expressed in kilometres from below the surface, i.e. the point of eruption on the volcano edifice, and then corrected relative to sea level. Ninety-seven percent of all MI show an entrapment depth of between 1 and 6 km. Just 3% show slightly deeper entrapment depths of up to 9 km. The uncertainty on each MI depth is ~±600 m, based on typical accuracy of calculated MI pressures of ±22 MPa (Blundy and Cashman 2008) and an uncertainty of ~10% on the assumed crustal density. These estimates of uncertainty do not take into account any systematic bias induced from the use of VolatileCalc to obtain pressures from peralkaline liquids (see above).

In summary, the MI data indicate a shallow magma storage area which is vertically extensive over ~4 km, at temperatures of ≥700°C. Crystallisation was driven primarily by cooling under vapour-saturated conditions. The vapour was a mixed H_2O–CO_2 fluid, with H_2O/CO_2 increasing with crystallisation at any given depth. Cl data suggest that a brine phase may have also been present, although this has not been observed petrographically. A single MI with high CO_2 yields a pressure of 284 MPa, which might represent the melt intruded into the shallow storage region.

Discussion

Having established the storage conditions of pantellerite magma prior to the most recent eruptions from Dabbahu, it is instructive to compare the storage depths with estimates from seismology and InSAR, to assess whether current volcanic unrest could involve magmas sourced from a similar system

Comparison to seismic data

Following the September 2005 tectono-magmatic event, a seismic array of six broad-band seismometers was deployed in October 2005 around the Dabbahu and Manda Hararo magmatic segments, including three seismometers around the Da'Ure eruption site (Ebinger et al. 2008). This temporary array recorded a total of 1,939 earthquakes throughout the area, between Oct 2005 and April 2006, 485 of which were associated with the ~25 km^2 region around Dabbahu. Earthquake locations and S-wave attenuation beneath volcanoes have long been used to suggest the presence of magma, e.g. (Einarsson 1978; Feuillet et al. 2004). Earthquakes are typically thought to occur around the margins of magma chambers, triggered by high pore pressures in the aureole.

The Dabbahu earthquakes were calculated to depth below surface, the surface being defined as a mean datum taken from the elevation of the highest station (745 masl). The uncertainty on each earthquake depth is ~±500 m. In order to compare MI depths to earthquake depths, a correction to sea-level was applied to both data sets.

The MI and earthquake data (recalculated to the same planar surface) show a good correlation (Fig. 9) despite the time gap (up to ~8 kyr), between the eruption of the obsidian samples, and the 2005–2006 earthquake data. The MI are contained within the depth span of the earthquakes which should preferentially lie at the margins of the three-dimensional magma storage region. The recorded earthquakes at Dabbahu are interpreted as deformation following the magma extraction during 2005 dyke injection event (Ebinger et al. 2008). A plan-view of the data for a specified depth range (Fig. 10), clearly indicates a central earthquake-free void between 2 and 6 km, interpreted as an area of magma storage. The eruption source point for sample 055, easily located from satellite imagery, plots directly above this area. Abundant earthquakes above 2 km are suggestive of a fractured roof above the magma chamber. Below 6 km, the earthquakes are less frequent, and the presence of magma storage cannot be clearly defined. Ebinger et al. (2008) suggest the hypocentral locations are indicative of a sill-like melt zone between 3 and 5 km depth. The correlation between seismic data and MI data suggests a consistency

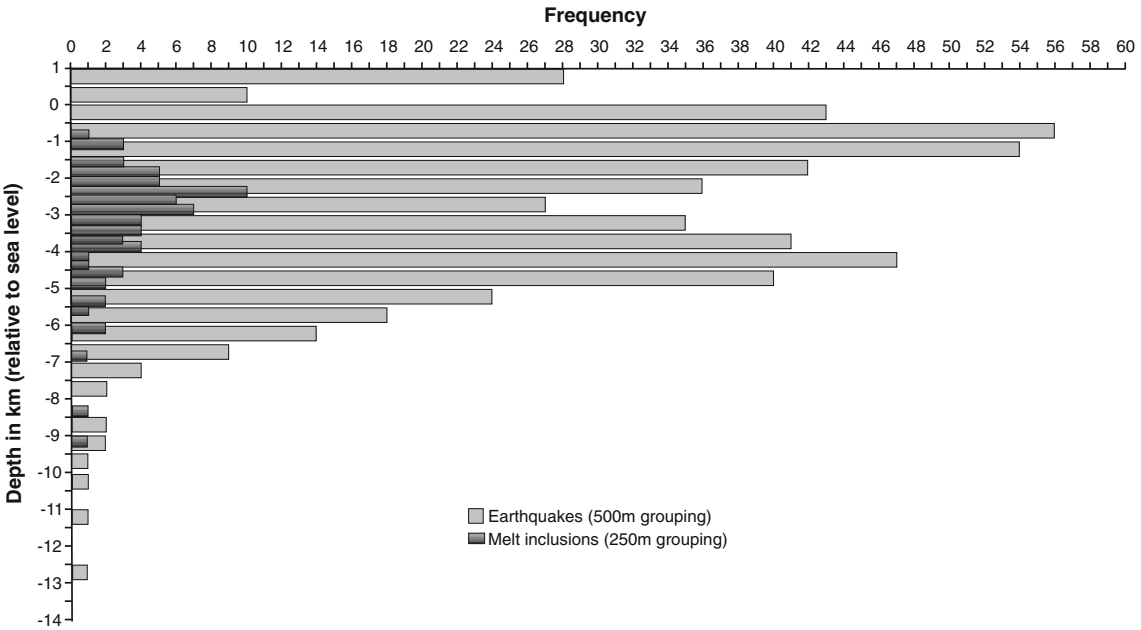

Fig. 9 Histogram illustrating melt inclusion saturation depths and earthquake hypocentre depths relative to sea level. Despite a time difference of up to 8 kyr, the petrologically determined magma storage depths show a reasonable correlation to depths of recent earthquakes beneath Dabbahu which record re-equilibration of the shallow magma storage region following magma evacuation related to the 2005 dyking event. Earthquake data from Ebinger et al. (2008)

in the magma storage beneath Dabbahu over the last few thousand years. This long-term stability may have contributed to the evolved nature of the most recent eruptive products.

Comparison to InSAR

InSAR data showed that Gab'ho, to the east of Dabbahu, began inflating after September 2000 and continued until the 2005 volcano-seismic crisis. Dabbahu itself did not inflate during this period (Wright et al. 2006). Two to three metres of deflation occurred around the Dabbahu and Gab'ho centres during the initial dyke intrusion and small Da'Ure vent eruption (Wright et al. 2006). Subsequent inflation is continuing and to date around ~0.5 m has been recovered at Dabbahu (Grandin et al. 2010).

The subsidence observed at Dabbahu in InSAR data during the 2005 dyke intrusion suggests that there is at least one major body of magma storage below Dabbahu controlling the measurable inflation and deflation (Wright et al. 2006). Regular InSAR acquisitions from the European Space Agency's Envisat satellite have enabled a large time-series of InSAR data to be built for the Dabbahu area since the 2005 event (Grandin et al. 2010; Hamling et al. 2010). Here, we carefully reanalyse InSAR data from Dabbahu, and since we are interested in the location and shape of the magmatic source, rather than temporal behaviour, interferograms with long time intervals were analysed to maximise the signal-to-noise ratio. Details of the InSAR data processing methods are provided in Online resource 2.

Surface deformation in the vicinity of Dabbahu responds to a variety of processes, including on-going dyke intrusions in the rift to the south (Hamling et al. 2009, 2010), viscoelastic relaxation (Nooner et al. 2009) and magmatic deformation at the Ado' Ale Volcanic complex, Gab'ho and Dabbahu itself (Grandin et al. 2010). The concern here is with relatively shallow processes occurring beneath Dabbahu. Therefore, we isolated the deformation associated with sources beneath Dabbahu by removing an interpolated deformation created from data more than 10 km away from Dabbahu (Fig. 11: Online resource 2).

The isolated shallow Dabbahu deformation interferograms show concentric range decreases approximately centred on Dabbahu. The maximum observed range decrease is 40 and 50 cm in ascending and descending interferograms, respectively. The concentric range decrease in the ascending interferogram is skewed to the west of that in the descending interferogram. This is consistent with an inflating source and suggests that the deformation consists of an uplift signal (causing range decrease in both ascending and descending interferograms) and horizontal deformation pointing radially outwards: To the east of Dabbahu, horizontal and vertical motion both result in range decreases for the descending pass; for the ascending pass in this location, the horizontal motion acts in the opposite direction to the vertical; the opposite is true west of Dabbahu.

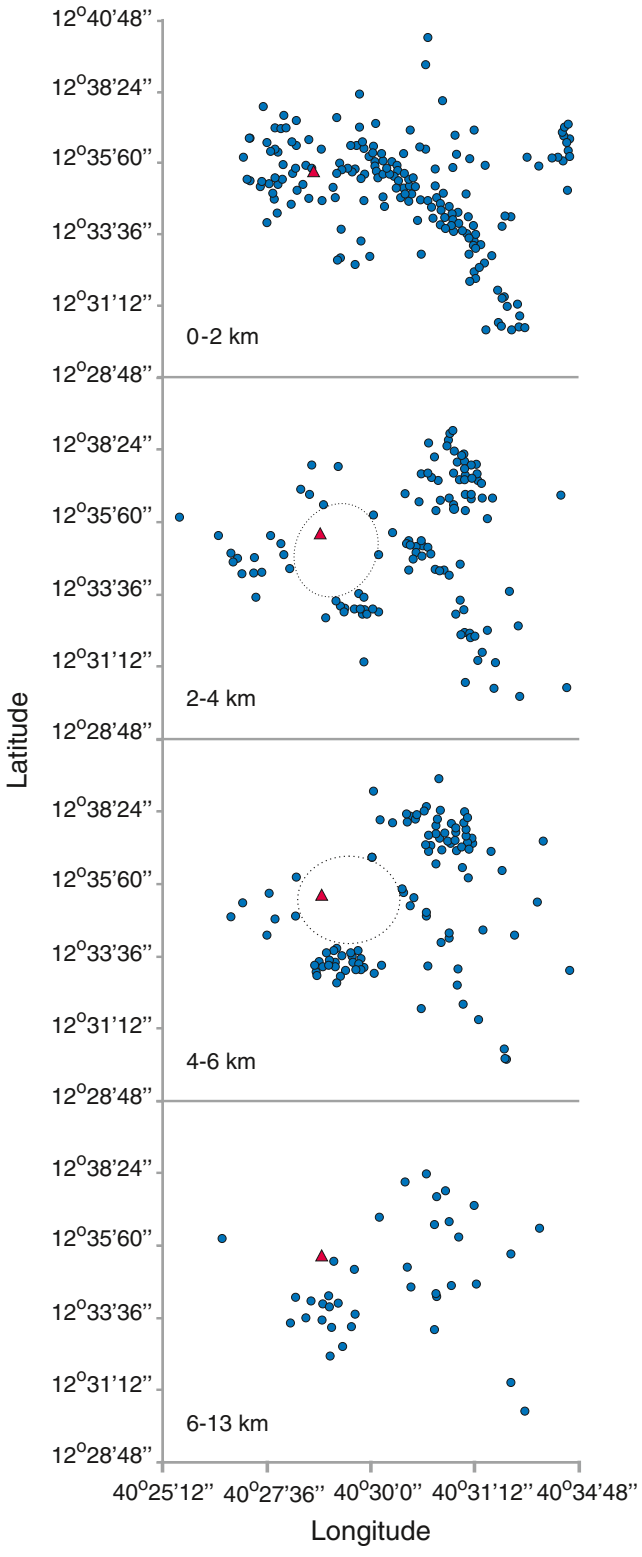

Fig. 10 Locations of Dabbahu earthquakes in plan-view for Oct 2005–Apr 2006 (*blue circles*) in three different depth slices (in kilometres below sea level). *Red triangle* (the eruptive vent of sample 055) corresponds to a central earthquake-free area roughly denoted by *dotted line ellipse* at 2–4 and 4–6 km depth slices. Scale and key are the same for all plots. Earthquake data from Ebinger et al. (2008)

Source modelling

Modelling of InSAR data is non-unique, requiring constraints on the shape of the magma body and the rheology of the surrounding rocks (e.g. Pritchard and Simons 2004). Here, we use the depth distribution of the MI to constrain magma chamber inflation models. The MI data suggest a vertically extensive magma chamber was tapped during eruptions over the last ~8 kyr, and it is instructive to see whether such a configuration can be matched to the InSAR observations, given the seismic evidence that the current eruptive phase has tapped a body located over a similar depth range.

As a baseline, two models were tested initially with the magma source at a single depth: (a) a point pressure source (Mogi 1958) and (b) a simple sill (Okada 1985). However, as petrological data suggest that the magma from historical eruptions was stored over an extended depth range, we tested two additional models: (c) a vertical ellipsoidal source (Yang et al. 1988), with a variety of aspect ratios, extending from a depth of 1.5 to 4.5 km, and (d) a stacked sills model, consisting of three sills at depths of 1.5, 3.0 and 4.5 km. In all cases, simple analytical solutions assumed an isotropic elastic half-space, and Poisson's ratio was fixed at 0.25.

We found that the best-fit, simple point source (model A) was at a depth of 3.0±0.1 km and inflated by 0.022±0.002 km^3, providing a reasonable fit to the observed deformation (Fig. 12a) with an rms misfit of 1.67 cm. However, the model over-predicts the deformation at large distances from the source. A sill (model B) with edge length 5.6±0.6 km at a depth of 3.5±0.4 km, opening by 0.7±0.3 m (volume change of 0.023±0.002 km^3) fits the observed interferograms significantly better than the point source, with an rms misfit of 1.11 cm. This is mainly because the deformation is more localised, fitting the far field of the deformation source better than the Mogi model (Fig. 12b).

Ellipsoidal sources (model C) were used to simulate a single magma chamber distributed over the depth range suggested by petrology (1–4.5 km). For a narrow, "cigar-shaped" ellipse, with a horizontal axis of half-length 0.1 km, a good fit to the observed data cannot be found (Fig. 12e)—the rms misfit is 2 cm, and the best-fit pressure change is unfeasibly large (370±20 MPa, assuming a shear modulus of 1,010 Pa). The fit to the data is improved as the length of the horizontal axis increases. A spherical chamber fits the data identically to the point Mogi source, with a more realistic pressure change of 20±1 MPa. The best-fit ellipsoid has a horizontal axis (half-length, 3.9 km) more than twice the length of the vertical axis with a pressure change of 2±0.1 MPa. The rms misfit for this solution was 1.5 cm: better than the Mogi source, but worse than the simple sill model. The presence of seismicity within this source geometry suggests that a magma chamber of this size and shape is not realistic and was therefore ruled out.

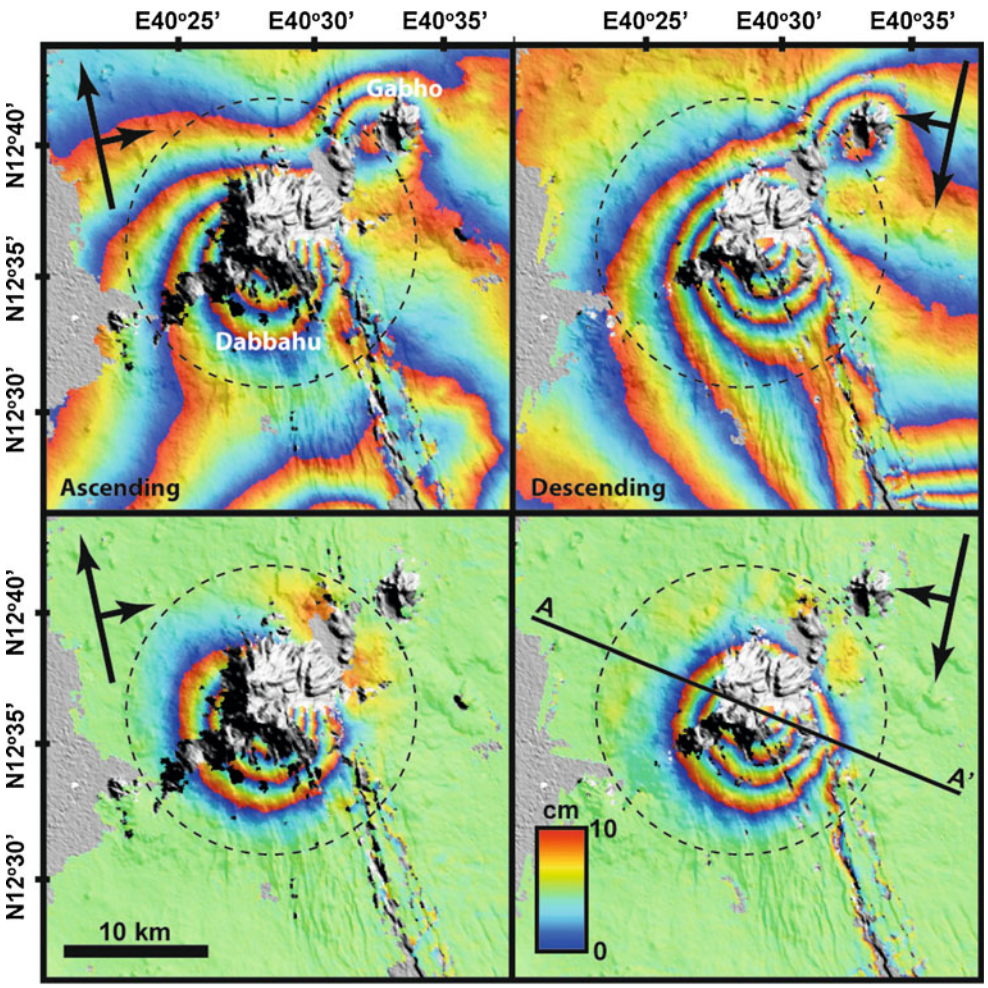

Fig. 11 The isolated InSAR signal for Dabbahu. Localised deformation around Dabbahu determined by subtracting the interpolated interferograms from the originals. *A-A'* is the section used for profile modelling in Fig. 11. The ascending interferogram is formed from acquisitions on 3 April 2006 and 1 February 2010, and the descending spans the interval from 21 April 2006 to 26 March 2010. They record the inflation signal following the 2005 event

An alternative plumbing system that will allow magma to be distributed over a large vertical extent is a system of stacked sills (model D), connected by a network of narrow conduits or dykes. Such a plumbing system has been proposed as a plausible geometry for magma storage and differentiation within the crust (e.g. Macdonald et al. 1995; Zellmer and Annen 2008). We constructed a simple system with three sills superimposed vertically on top of each other, at depths of 1.5, 3.0 and 4.5 km, and solved for the size and amount of opening for each sill. The majority of the volume-change 0.018±0.008 km^3 is found to occur in the sill at 3 km depth, which has an edge length of 7.1±3.5 km and opens by 0.36±0.18 m. The other sills both contributed ~0.0025±0.001 km^3 and have relatively narrow dimensions (1.6±0.6 km length and 1.6±1.6 m opening for the shallow source at 1.5 km; 1.3±1.3 km length and 1.6±2.7 m opening for the deep source at 4.5 km). The model parameters are strongly co-variant, both for parameters associated with individual sills and between the different sills, e.g. solutions with high volume change in the 3 km sill have low volume change in the 4.5 km sill. The rms misfit to the data of 1.08 cm is marginally better than the single sill, largely due to the shallow source allowing the deformation to fit the peak of the deformation pattern significantly better than the single sill model (Fig. 12c).

Although the stacked sills model is the best-fit solution, it would probably not have been selected above the simpler, single-sill model based on the deformation data alone. Given the additional constraint from petrology that the magma has historically been distributed between depths of ~1 and 5 km, distributing the magma through a series of stacked sills is consistent with the deformation data.

Conclusions

The bulk of the MI from Dabbahu are H_2O-rich, with between 3 and 5 wt.%, although the highest value measured was 5.8 wt.% H_2O. High magmatic H_2O is consistent with other findings in peralkaline rocks. The pumice and obsidian glasses have largely degassed prior to quenching. H_2O degassing does not appear to govern crystallisation at Dabbahu, which is instead driven by cooling. Major elements are buffered within the system, suggestive of near-eutectic behaviour. In contrast, trace element signatures are far more responsive to crystallisation.

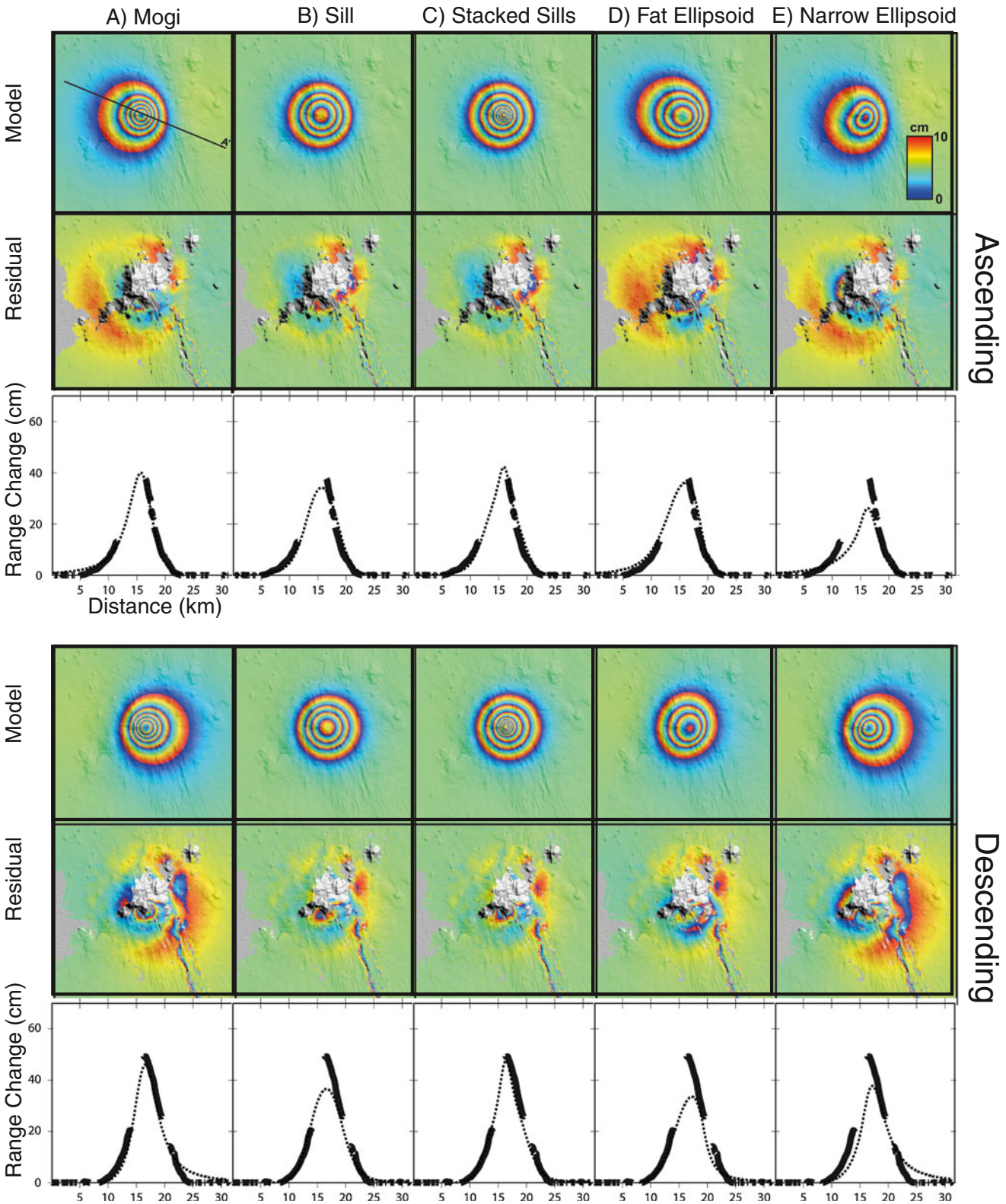

Fig. 12 Ascending and descending models and associated residuals for the Dabbahu InSAR signal (acquisition dates as for Fig. 10). Range-change profiles are modelled from *A-A'* as shown on the ascending Mogi model. Different models evaluated are described in the text

Indicated magma storage depths are shallow, which is in line with observations at other peralkaline volcanoes, but show a range of depths from ~1 to 6 km. This depth range is consistent with seismic data obtained during the current

tectonic–magmatic unrest. Using the petrological estimates of historical magma storage depths, we have attempted to fit the InSAR data. We find that a system of thin, stacked sills provides a good match to the deformation data. Utilising the three approaches (petrology, seismology and geodesy) has enabled us to constrain not only the depths of magma storage but also the geometry. The current magmatic activity at Dabbahu is consistent with storage of magma at similar depths to that involved in historical eruptions; it may currently be being refilled by new batches of magma, or reactivated by injections of basaltic magma as inferred for the recent (2005) eruption from the Da'Ure (Wright et al. 2006). We conclude that the magma storage system beneath Dabbahu has maintained a stable geometry of multiple stacked sills over the past few thousand years.

Acknowledgements This work has been supported by the Natural Environment Research Council, Afar Rift Consortium grant NE/F007604/1. The authors acknowledge the generous support of the University of Addis Ababa with fieldwork arrangements, particularly E. Lewi and A. Ayele, and the Afar Regional Government for invaluable assistance. Detailed Dabbahu earthquake data were kindly provided by C. Ebinger. The authors gratefully acknowledge technical assistance provided by S. Kearns (EMPA), R. Hinton and J. Craven (SIMS), N. Marsh and R. Kelly (XRF) and thorough reviews by J. Lowenstern and R. MacDonald.

References

Anderson AT, Brown GG (1993) CO2 contents and formation pressures of some Kilauean melt inclusions. Am Min 78(7–8):794–803

Ayele A, Jacques E, Kassim M, Kidane T, Omar A, Tait S, Nercessian A, de Chabalier J, King G (2007) The volcano-seismic crisis in Afar, Ethiopia starting September 2005. Earth Planet Sci Lett 255 (1–2):177–187

Ayele A, Keir D, Ebinger C, Wright TJ, Stuart GW, Buck WR, Jacques E, Ogubazghi G, Sholan J (2009) September 2005 mega-dike emplacement in the Manda-Harraro nascent oceanic rift (Afar depression). Geophys Res Lett 36

Bailey DK, Macdonald R (1969) Alkali-feldspar fractionation trends and derivation of peralkaline liquids. Am J Sci 267(2):242–248

Bailey DK, Cooper JP, Knight JL (1974) Anhydrous melting and crystallization of peralkaline obsidians. Bull Volcanol 38 (2):653–665

Barberi F, Varet J (1977) Volcanism of Afar—small-scale plate tectonic implications. Geol Soc Am Bull 88(9):1251–1266

Barberi F, Ferrara R, Santacroce R, Treuil M, Varet J (1974a) A transitional basalt—pantellerite sequence of fractional crystallisation, the Boina centre, (Afar Rift, Ethiopia). J Petrol 16(1):22–56

Barberi F, Santacroce R, Varet J (1974b) Silicic peralkaline volcanic rocks of the Afar Depression (Ethiopia). Bull Volcanol 38(2):755–790

Barclay J, Carroll MR, Houghton BF, Wilson CJN (1996) Pre-eruptive volatile content and degassing history of an evolving peralkaline volcano. J Volcanol Geotherm Res 74(1–2):75–87

Bizouard H, Barberi F, Varet J (1980) Mineralogy and petrology of Erta Ale and Boina volcanic series, Afar Rift, Ethiopia. J Petrol 21 (2):401–436

Blundy J, Cashman K (2005) Rapid decompression-driven crystallization recorded by melt inclusions from Mount St. Helens volcano. Geology 33(10):793–796

Blundy J, Cashman K (2008) Petrologic reconstruction of magmatic system variables and processes. In: FJ PKT (ed) Minerals, inclusions and volcanic processes. Min Soc Am, 3635 Concorde Pkwy STE 500, Chantilly, VA 20151-1125 USA pp 179–239

Bürgmann R, Rosen PA, Fielding EJ (2000) Synthetic aperture radar interferometry to measure earth's surface topography and its deformation. Annu Rev Earth Planet Sci 28(1):169–209

Cornwell DG, Mackenzie GD, England RW, Maguire PKH, Asfaw LM, Oluma B (2006) Northern main Ethiopian rift crustal structure from new high-precision gravity data. Geol Soc Lond Spec Pub 259(1):307–321

Danyushevsky LV, Della Pasqua FN, Sokolov S (2000) Re-equilibration of melt inclusions trapped by magnesian olivine phenocrysts from subduction-related magmas; petrological implications. Contribu Min Petrol 138(1):68–83

Di Carlo I, Rotolo SG, Scaillet B, Buccheri V, Pichavant M (2010) Phase equilibrium constraints on pre-eruptive conditions of recent felsic explosive volcanism at Pantelleria Island, Italy. J Petrol 51:2245–2276

Dixon JE (1997) Degassing of alkalic basalts. Am Min 82(3–4):368–378

Ebinger C, Keir D, Ayele A, Calais E, Wright TJ, Belachew M, Hammond JOS, Campbell E, Buck WR (2008) Capturing magma intrusion and faulting processes during continental rupture: seismicity of the Dabbahu (Afar) rift. Geophys J Int 174:1138–1152

Einarsson P (1978) S-wave shadows in the Krafla Caldera in NE-Iceland, evidence for a magma chamber in the crust. Bull Volcanol 41(3):187–195

Feuillet N, Nostro C, Chiarabba C, Cocco M (2004) Coupling between earthquake swarms and volcanic unrest at the Alban Hills Volcano (central Italy) modeled through elastic stress transfer. J Geophys Res-Solid Earth 109(B2)

Gioncada A, Landi P (2010) The pre-eruptive volatile contents of recent basaltic and pantelleritic magmas at Pantelleria (Italy). Bull Volcanol 189:191–201

Grandin R, Socquet A, Doin MP, Jacques E, de Chabalier JB, King GCP (2010) Transient rift opening in response to multiple dike injections in the Manda Hararo rift (Afar, Ethiopia) imaged by time-dependent elastic inversion of interferometric synthetic aperture radar data. J Geophys Res 115 B:B09403

Hamling IJ, Ayele A, Bennati L, Calais E, Ebinger CJ, Keir D, Lewi E, Wright TJ, Yirgu G, (2009) Geodetic observations of the ongoing Dabbahu rifting episode: new dyke intrusions in 2006 and 2007. Geophys J Int 178:989–1003

Hamling IJ, Wright TJ, Calais E, Bennati L, Lewi E (2010) Stress transfer between thirteen successive dyke intrusions in Ethiopia. Nature Geosci 3:713–717

Hill GJ, Caldwell TG, Heise W, Chertkoff DG, Bibby HM, Burgess MK, Cull JP, Cas RAF (2009) Distribution of melt beneath Mount St Helens and Mount Adams inferred from magnetotelluric data. Nat Geosci 2(11):785–789

Horn S, Schmincke HU (2000) Volatile emission during the eruption of Baitoushan Volcano (China/North Korea) ca. 969 AD. Bull Volcanol 61(8):537–555

Humphreys MCS, Kearns SL, Blundy JD (2006) SIMS investigation of electron-beam damage to hydrous, rhyolitic glasses: implications for melt inclusion analysis. Am Min 91(4):667–679

Lahitte P, Gillot P, Courtillot V (2003) Silicic central volcanoes as precursors to rift propagation; the Afar case. Earth Planet Sci Lett 207(1–4):103–116

Lees JM (2007) Seismic tomography of magmatic systems. J Volcanol Geotherm Res 167(1–4):37–56

Lowernstern JB, Mahood GA (1991) New data on magmatic H2O contents of pantellerites with implications for petrogenesis and eruptive dynamics at Pantelleria. Bull Volcanol 54:78–83

Macdonald R (1974) Nomenclature and petrochemistry of the peralkaline oversaturated extrusive rocks. Bull Volcanol 38 (2):498–516

Macdonald R et al (1995) Petrogenesis of Silali volcano, Gregory Rift, Kenya. J Geol Soc 152:703–720

Macdonald R et al (2011) Mineral stability in peralkaline silicic rocks: Information from trachytes of the Menengai volcano, Kenya. Lithos 125:553–568

Mahatsente R, Jentzsch G, Jahr T (1999) Crustal structure of the Main Ethiopian Rift from gravity data: 3-dimensional modeling. Tectonophysics 313(4):363–382

Marshall AS et al (1998) Phenocrystic fluorites in peralkaline rhyolites, Olkaria, Kenya Rift Valley. Min Mag 62:477–486

Metrich N, Rutherford MJ (1992) Experimental study of chlorine behaviour in hydrous silicic melts. Geochim Et Cosmochim Acta 56(2):607–616

Metrich N, Wallace PJ (2008) Volatile abundances in basaltic magmas and their degassing paths tracked by melt inclusions. In: Putirka K, Tepley FJ (eds) Annual Fall American-Geophysical-Union Meeting. Min Soc Amer, San Franscisco, pp 363–402

Mickus K, Tadesse K, Keller GR, Oluma B (2007) Gravity analysis of the main Ethiopian rift. J Afr Earth Sci 48(2–3):59–69

Mogi K (1958) Relations between the eruptions of various volcanoes and the deformations of the ground surfaces around them. Bulletin of the Earthquake Research Institute 36:99–134

Newman S, Lowenstern JB (2002) VolatileCalc: a silicate melt-H2O-CO2 solution model written in Visual Basic for excel. Comput Geosci 28(5):597–604

Newman S, Stolper EM, Epstein S (1986) Measurement of water in rhyolitic glasses: calibration of an infrared spectroscopic technique. Am Min 71:1527–1541

Nicholls J, Carmichael ISE (1969) Peralkaline acid liquids: a petrological study. Contrib Min Petrol 20(3):268–294

Nielsen RL, Michael PJ, Sours-Page R (1998) Chemical and physical indicators of compromised melt inclusions. Geochim Et Cosmochim Acta 62(5):831–839

Nooner SL, Bennati L, Calais E, Buck WR, Hamling IJ, Wright TJ, Lewi E (2009) Post-rifting relaxation in the Afar region, Ethiopia. Geophys Res Lett 36:L21308

Okada Y (1985) Surface deformation due to shear and tensile faults in a half-space. Bulletin of the Seismological Society of America, 75:1135–1154

Papale P, Moretti R, Barbato D (2006) The compositional dependence of the saturation surface of H2O + CO2 fluids in silicate melts. Chem Geol 229(1–3):78–95

Pritchard ME, Simons M (2002) A satellite geodetic survey of large-scale deformation of volcanic centres in the central Andes. Nature 418(6894):167–171

Pritchard ME, Simons M (2004) An InSAR-based survey of volcanic deformation in the central Andes. Geochem Geophys Geosyst 5: Q02002

Putirka KD (2008) Thermometers and barometers for volcanic systems. Minerals, inclusions and volcanic processes. Rev Min Geochem 69:61–120

Rowland J, Baker E, Ebinger C, Keir D, Kidane T, Biggs J, Hayward N, Wright TJ (2007) Fault growth at a nascent slow-spreading ridge: 2005 Dabbahu rifting episode, Afar. Geophys J Int 171 (3):1226–1246

Sasai Y (1991) Piezomagnetic field associated with the Mogi model revisited—analytic solution for finite spherical source. J Geomagn Geoelectr 43(1):21–64

Scaillet B, Macdonald R (2001) Phase relations of peralkaline silicic magmas and petrogenetic implications. J Petrol 42(4):825–845

Scaillet B, Macdonald R (2003) Experimental constraints on the relationships between peralkaline rhyolites of the Kenya rift valley. J Petrology 44(10):1867–1894

Scaillet B, Macdonald R (2006) Experimental constraints on pre-eruption conditions of pantelleritic magmas: evidence from the Eburru complex, Kenya Rift. Lithos 91(1–4):95–108

Schumacher JC (1991) Empirical ferric iron correction-necessity, assumptions, and effects on selected geothermobarometers. Mineral Mag 55:3–18

Shalev E, Kenedi CL, Malin P, Voight V, Miller V, Hidayat D, Sparks RSJ, Minshull T, Paulatto M, Brown L, Mattioli G (2010) Three-dimensional seismic velocity tomography of Montserrat from the SEA-CALIPSO offshore/onshore experiment. Geophys Res Lett 37

Tamic N, Behrens H, Holtz F (2001) The solubility of H2O and CO2 in rhyolitic melts in equilibrium with a mixed CO2-H2O fluid phase. Chem Geol 174(1–3):333–347

Thompson RN, Mackenzie WS (1967) Feldspar-liquid equilibria in peralkaline acid liquids—an experimental study. Am J Sci 265 (8):714–734

Webster J, Taylor RP, Bean C (1993) Pre-eruptive melt composition and constraints on degassing of a water-rich pantellerite magma, Fantale volcano. Ethiopia Contrib Min Petrol 114:1

Whaler KA, Hautot S (2006) The electrical resistivity structure of the crust beneath the northern Main Ethiopian Rift. In: Yirgu G, Ebinger CJ, Maguire PKH (eds) Afar volcanic province within the East African rift system pp 293–305

White JC, Holt GS, Parker DF, Ren MH (2003) Trace-element partitioning between alkali feldspar and peralkalic quartz trachyte to rhyolite magma. Part I: systematics of trace-element partitioning. Am Min 88(2–3):316–329

White JC, Ren M, Parker DF (2005) Variation in mineralogy, temperature and oxygen fugacity in a suite of strongly peralkaline lavas and tuffs, Pantelleria, Italy. Can Min 43:1331–1347

Wilding MC, MacDonald R, Davies JE, Fallick AE (1993) Volatile characteristics of peralkaline rhyolites from Kenya: an ion microprobe, infrared spectroscopic and hydrogen isotope study. Contrib Min Petrol 114(2):264–275

Williams-Jones G, Rymer H, Mauri G, Gottsmann J, Poland M, Carbone D (2008) Toward continuous 4D microgravity monitoring of volcanoes. Geophysics 73(6):WA19–WA28

Wolfenden E, Ebinger C, Yirgu G, Renne PR, Kelley SP (2005) Evolution of a volcanic rifted margin: Southern Red Sea, Ethiopia. Geol Soc Am Bull 117(7–8):846–864

Wright TJ (2002) Remote monitoring of the earthquake cycle using satellite radar interferometry. Phil Trans R Soc Lond Series A: Math, Phys Eng Sci 360(1801):2873–2888

Wright TJ, Ebinger CJ, Biggs J, Ayele A, Yirgu G, Keir D, Stork A (2006) Magma maintained rift segmentation at continental rupture in the 2005 Afar dyking episode. Nature 442:291–294

Yang X-M, Davis PM, Dieterich JH (1988) Deformation from inflation of a dipping finite prolate spheroid in an elastic half-space as a model for volcanic stressing. J Geophys Res 93:4249–4257

Zellmer G, Annen C (2008) An introduction to magma dynamics (in Dynamics of crystal magma transfer, storage and differentiation). Geol Soc Spec Publ 304:1–13